EDGE ARTICLE

Check for updates

Structure and solvation of confined water and water–ethanol clusters within microporous Brønsted acids and their effects on ethanol dehydration catalysis†

Jason S. Bates, ‡ Brandon C. Bukowski, ‡ Jeffrey Greeley *
and Rajamani Gounder *

Aqueous-phase reactions within microporous Brønsted acids occur at active centers comprised of water-reactant-clustered hydronium ions, solvated within extended hydrogen-bonded water networks that tend to stabilize reactive intermediates and transition states differently. The effects of these diverse clustered and networked structures were disentangled here by measuring turnover rates of gas-phase ethanol dehydration to diethyl ether (DEE) on H-form zeolites as water pressure was increased to the point of intrapore condensation, causing protons to become solvated in larger clusters that subsequently become solvated by extended hydrogen-bonded water networks, according to *in situ* IR spectra. Measured first-order rate constants in ethanol quantify the stability of S_N2 transition states that eliminate DEE relative to $(C_2H_5OH)(H^+)(H_2O)_n$ clusters of increasing molecularity, whose structures were respectively determined using metadynamics and *ab initio* molecular dynamics simulations. At low water pressures (2–10 kPa H_2O), rate inhibition by water (−1 reaction order) reflects the need to displace one water by ethanol in the cluster en route to the DEE-formation transition state, which resides at the periphery of water–ethanol clusters. At higher water pressures (10–75 kPa H_2O), water–ethanol clusters reach their maximum stable size $((C_2H_5OH)(H^+)(H_2O)_{4-5})$, and water begins to form extended hydrogen-bonded networks; concomitantly, rate inhibition by water (up to −3 reaction order) becomes stronger than expected from the molecularity of the reaction, reflecting the more extensive disruption of hydrogen bonds at DEE-formation transition states that contain an additional solvated non-polar ethyl group compared to the relevant reactant cluster, as described by non-ideal thermodynamic formalisms of reaction rates. Microporous voids of different hydrophilic binding site density (Beta; varying H^+ and Si−OH density) and different size and shape (Beta, MFI, TON, CHA, AEI, FAU), influence the relative extents to which intermediates and transition states disrupt their confined water networks, which manifest as different kinetic orders of inhibition at high water pressures. The confinement of water within sub-nanometer spaces influences the structures and dynamics of the complexes and extended networks formed, and in turn their ability to accommodate the evolution in polarity and hydrogen-bonding capacity as reactive intermediates become transition states in Brønsted acid-catalyzed reactions.

1. Introduction

In heterogeneous catalysis, the interface between liquid or liquid-like solvating environments and active sites at solid surfaces can significantly alter reaction rates and selectivities,[1] and its ubiquitous effects have been documented in electrocatalysis,[2–6] aqueous-phase reactions on metal nanoparticles,[7–12]

Charles D. Davidson School of Chemical Engineering, Purdue University, 480 Stadium Mall Drive, West Lafayette, IN 47907, USA. E-mail: jgreeley@purdue.edu; rgounder@purdue.edu

† Electronic supplementary information (ESI) available. See DOI: 10.1039/d0sc02589e

‡ J. S. B. and B. C. B. contributed equally to this work.

and gas-phase reactions at high pressures sufficient to cause condensation within porous solids (*e.g.*, Fischer–Tropsch synthesis[13–16] and alkene oligomerization[17–19]). In addition, confinement within sub-nanometer spaces imposes constraints on the structures that solvents can adopt, and in turn their influence on reactive intermediates and transition states stabilized at active sites, as demonstrated by the breadth of water structures and dynamics within carbon nanotubes of different dimensions,[20–23] and the diverse function of enzymes with different hydrophobicity.[24] Inorganic, crystalline, microporous frameworks offer independent synthetic control of the density, chemical identity, and coordination of catalytic active sites, and the structure and polarity of the environments that

confine them, which make zeolites and zeotype-molecular sieves a versatile platform to study fundamental principles underlying the structure and catalytic behavior of confined solvents. Lewis acid zeolites containing framework Ti^{4+} or Sn^{4+} centers have been reported recently to show significant differences in reactivity for aqueous-phase olefin epoxidation[25–29] and sugar isomerization[30–34] in response to changes in active site structure and the stabilization or exclusion of extended water networks within microporous environments. The interplay between the solvated structures and reactivity of Brønsted acidic H^+ sites associated with framework Al^{3+} in siliceous zeolites (Si–O(H^+)–Al), however, are less well-understood because of the greater diversity of H^+, reactant, and transition state complexes engendered by solvating water within confining voids.

Zeolite frameworks are comprised primarily of siloxane bonds that are non-polar and hydrophobic,[35] but they also contain hydrophilic binding sites in the form of H^+ sites and defect Si–OH groups that preferentially bind H_2O.[35–38] At low coverages (<1 H_2O per H^+), H_2O forms hydrogen-bonded complexes with H^+ sites;[39,40] as additional H_2O molecules adsorb (>1 H_2O per H^+), hydronium ions (H_3O^+) form.[41,42] Vjunov et al.[43] reported IR spectra, DFT calculations, and Al K-edge XANES spectra of H-Al-MFI zeolites that indicate formation of $H^+(H_2O)_n$ clusters analogous to those present in gaseous phases, which causes delocalization of the positive charge away from the charge-compensating framework $[AlO_{4/2}]^-$. The molecularity of these $H^+(H_2O)_n$ clusters, determined from vapor-phase H_2O adsorption isotherms (298 K) on H-Al-MFI samples of varying H^+ content (Si/Al = 15–110), was reported to be 7–8 H_2O per H^+; this stoichiometry is consistent with aqueous-phase cyclohexanol adsorption saturation uptakes (298 K) that decrease with increasing H^+ content as $H^+(H_2O)_{7-8}$ clusters occupy higher fractions of available void space.[44] The stoichiometry of 7–8 H_2O per cluster was also corroborated by ^1H and ^1H–^{29}Si CP MAS NMR spectra of H-Al-MFI (Si/Al = 15, 40) samples as a function of H_2O coverage (at ambient temperature) and by ab initio molecular dynamics (AIMD) simulations (at 300 K).[45] These results highlight not only the distinct clustered structures of H_2O stabilized at H^+ sites located within the confined sub-nanometer spaces of zeolites, unlike the classical solution-phase Zundel ($H_5O_2^+$)[46] and Eigen ($H_9O_4^+$)[47] structures or the $H_{13}O_6^+$ cluster reported by Stoyanov et al.,[48] but also the more compressed structures and different proton-hopping dynamics than gas-phase clusters according to AIMD simulations.[45] Despite these detailed structural characterizations of $H^+(H_2O)_n$ in confined spaces, changes to their structure upon interacting with reactants under conditions relevant to catalysis, and the kinetic consequences of such solvated reactant and transition state complexes, are not as well-understood.

Solvent effects in reactions catalyzed by Brønsted acid zeolites have been studied at the extremes of low solvent pressures that form gas-like species, and of high solvent pressures that form liquid-like species, but seldom integrate insights from these disparate surface coverage regimes into a cohesive kinetic and mechanistic description of the catalytic chemistry. Haw and coworkers reported that co-solvating nitromethane enhanced the extent of gas-phase proton-transfer from H-Al-MFI to ^{13}C-labeled acetone detected by ^{13}C NMR, which enabled acetone dimerization only when nitromethane was co-fed in a flow reactor (513 K).[49] These concepts can be extended to co-adsorbed H_2O, which enhances gas-phase rates of alkane C–H bond activation,[50] H–D exchange,[51] and steam dealumination[52] in H-zeolites, and enables distinct H_3O^+-mediated pathways in aqueous-phase hydrogenation of furanics[53] and aldol condensation of ketones.[54] In gas-phase alcohol dehydration reactions, H_2O inhibits the rates of forming both alkenes and ethers in unimolecular and bimolecular pathways, respectively.[55] H_2O inhibition quantified by negative reaction orders is often described by reaction mechanisms that include inhibitory alcohol–water dimer species, as observed in alcohol dehydration catalyzed by Brønsted acidic Keggin-type polyoxometalate clusters[56] and Lewis acidic γ-Al_2O_3 [57,58] and Sn-Beta zeolites.[59,60] Others have suggested that co-adsorbed H_2O inhibits alcohol dehydration by stabilizing adsorbed alcohols preferentially over transition states, in the case of 1-propanol dehydration on H-Al-MFI zeolites.[61] In the liquid phase, confinement of H_3O^+ within H-Al-Beta zeolite pores (~0.7 nm in diameter) leads to higher rates of cyclohexanol dehydration than in bulk solution, because of enhanced association between H_3O^+ and reactants and the entropic destabilization of this precursor relative to the transition state,[62] and solvation of H^+ by non-polar solvents rather than water leads to higher rates of phenol alkylation.[63] Kinetic and adsorption measurements showed that increasing densities of H_3O^+ resulted in lower reactant coverages at H_3O^+ active sites in aqueous-phase alkylation of phenol in H-Al-MFI zeolites (523 K),[64] and NMR measurements performed in operando showed that tuning organic/aqueous solvent compositions could change reactant coverages during glucose isomerization catalysis (403 K) within Na-FAU zeolites.[65] Turnover rates of homogeneously catalyzed unimolecular dehydration reactions, measured under conditions that reflect the stability of elimination transition states relative to the solvated proton, indicate that the composition of the H_2O–organic solvent mixture predominantly influences the free energy of the solvated proton, which is stabilized when solvated by water[66,67] and which influences selectivity when reactants are able to undergo parallel unimolecular pathways.[68] Equilibrium constants to protonate pyridine (293 K) within zeolites differ when their pores are filled by solvents of different polarity, also highlighting the important role of proton-solvent complex stability.[69] Other studies of co-solvents within zeolites, based on IR spectra and gas-phase isopropanol dehydration probe reactions, suggest that the protic nature of solvents (e.g., acetic acid) and co-existing cations (e.g., Na^+) can change the type, number, and strength of Brønsted acid sites in zeolites.[70–72] Bridging the gap in mechanistic understanding from that of molecular species and complexes prevalent during gas-phase studies at H_2O pressures well below saturation, to those of extended solvent networks and condensed phases around active sites that prevail during liquid-phase studies, requires considering how the clustered nature of alcohol–water intermediates at active sites evolves with the structure of solvating water networks confined within the same pores.[73,74] In

contrast to gas-phase studies, however, the scope of mechanistic investigations in heterogeneous catalysis is limited in liquid phases because aqueous solvent structures at the liquid–solid interface cannot be varied independently of reactant or co-solvent concentrations.

Here, we combine theoretical simulations with experimental kinetic measurements and *in situ* IR spectroscopy to obtain molecular-level insights into the structures of water and water–ethanol clusters and extended networks confined within micropores of different sizes and shapes, and their resulting effects on Brønsted acid catalysis. A suite of H-Al-Beta zeolites were synthesized with a wide range of H$^+$ densities (0.11–2.0 per unit cell) and Si–OH defects (~0.3–5 per unit cell) to obtain inorganic microporous materials with well defined densities of hydrophilic binding sites that can be used to interrogate the structures of adsorbed H$_2$O. Different H$_2$O structures are stabilized at H$^+$ and Si–OH groups within Beta zeolites, as probed by volumetric adsorption isotherms and their isosteric heats of adsorption, and by *in situ* IR spectra under conditions relevant to ethanol dehydration catalysis. Turnover rates of ethanol dehydration to diethyl ether (373 K, per H$^+$) are measured across a wide range of H$_2$O pressures (0.02–75 kPa) that encompass intrapore coverage regimes including alcohol–water dimers, alcohol–water–hydronium ion clusters, and extended hydrogen-bonded water networks that solvate them. Experimental turnover rates are interpreted mechanistically, aided by identifying the structures of most abundant reactive intermediates (MARI) by AIMD simulations and of kinetically relevant transition states by DFT calculations and metadynamics simulations. Interactions of transition states and precursors with extended hydrogen-bonded water networks manifest as inhibitory effects of H$_2$O on ethanol dehydration rates, which are much stronger than predicted by the molecularity of the reaction and require non-ideal thermodynamic formalisms to describe. This approach is also extended to microporous Brønsted acids with varying pore architectures, highlighting how the shapes of confining environments influence the structure and reorganization of solvents around reactive intermediates and transition states in Brønsted acid catalysis.

2. Results and discussion

2.1. Kinetics of Brønsted acid-catalyzed ethanol dehydration and water inhibition in zeolites

Different densities of Brønsted acid H$^+$ or Si–OH groups within zeolites stabilize water networks of distinct clustered and extended hydrogen-bonded structures,[43–45,75] which have been reported to influence reactivity in numerous ways, including different competitive adsorption of solvent(s) and reactants,[64,65] entropic gains when water networks are disrupted by transition states,[28,76] and entropic losses when transition states are disrupted by water networks.[34] Thus, interrogation of H-zeolite samples with varying H$^+$ and Si–OH density is required to disentangle their separate effects on intrapore solvent structure, prior to relating systematically varying solvent structures to the rate and equilibrium constants of a probe reaction catalyzed by H$^+$ sites, such as bimolecular ethanol dehydration to diethyl ether (DEE). Here, a suite of Brønsted acidic H-Al-Beta zeolites was synthesized in fluoride medium according to Camblor *et al.*[77] (denoted H-Al-Beta-F(*X*), where *X* is the number of H$^+$ per unit cell (u.c.$^{-1}$) determined by NH$_3$ TPD, Table 1). The use of fluoride as the mineralizing agent enabled preparing zeolites containing a wide range of proton densities (0.1–2 H$^+$ u.c.$^{-1}$) while minimizing the number of silanol defects (~0.3–0.6 Si–OH u.c.$^{-1}$, quantified by CD$_3$CN IR on Ti-Beta-F zeolites[34]) that otherwise form when hydroxide is used as the mineralizing agent (~3–5 Si–OH u.c.$^{-1}$, quantified by CD$_3$CN IR on Ti-Beta-OH zeolites[34]), because anionic siloxy (Si–O$^-$) defects form to balance the cationic charge of occluded tetraethylammonium cations in as-synthesized solids.[78] The H-Al-Beta-F samples in Table 1 therefore provide control of the density of H$^+$ sites within otherwise hydrophobic siliceous zeolite channels, whereas an H-Al-Beta-OH sample was synthesized in hydroxide medium to contain a higher density of Si–OH defects within micropores.

Turnover rates (373 K, per H$^+$) of ethanol dehydration to DEE were measured in differential reactors (details in Section S.2.1, ESI†) across a wide range of ethanol and water pressures (2 × 10^{-3} to 10 kPa C$_2$H$_5$OH, 0–75 kPa H$_2$O, Fig. 1) in order to quantify the effects of co-fed H$_2$O pressure in terms of rate constants that reflect the stabilities of intermediates and transition states in accepted reaction mechanisms. Such rate data were measured on

Table 1 Elemental compositions, micropore volumes, and H$^+$ densities of H-Al-Beta-F and their dealuminated analogs

Sample	Si/Al^a	$V_{micro}{}^b$/cm^3 g^{-1}	H$^+$/Al (NH$_4{}^+$)^c	H$^+$/Al (DTBP)^d	H^{+c}/u.c.	$V_{micro}{}^b$ (de-Al)^e
Si-Beta-F	—	0.21	—	—	0	—
H-Al-Beta-F(2.0)	23	0.22	0.75	0.54	2.0	0.22
H-Al-Beta-F(1.4)	34	0.18	0.78	—	1.4	0.21
H-Al-Beta-F(1.2)	45	0.20	0.84	0.79	1.2	0.21
H-Al-Beta-F(0.78)	65	0.21	0.79	—	0.78	0.20
H-Al-Beta-F(0.57)	93	0.23	0.84	—	0.57	0.22
H-Al-Beta-F(0.16)	220	0.20	0.54	1.1	0.16	—
H-Al-Beta-F(0.11)	500	0.20	0.84	—	0.11	—
H-Al-Beta-OH(1.7)	40	0.23	1.1	0.38	1.7	—

^{a} Determined by AAS. ^{b} Determined by minimum in $\partial V_{ads}/\partial \log(P/P_0)$ in N$_2$ adsorption isotherms. ^{c} Determined by TPD of NH$_3$ after aqueous-phase ion exchange with 1 M NH$_4$NO$_3$, 24 h, 353 K. ^{d} Determined by *in situ* 2,6-di-*tert*-butylpyridine titration during ethanol dehydration catalysis (378 K, 5 kPa C$_2$H$_5$OH, 1 kPa H$_2$O). ^{e} "de-Al" reflects deAl-Beta samples generated by treatment of H-Al-Beta in 69% HNO$_3$ (353 K, 16 h).
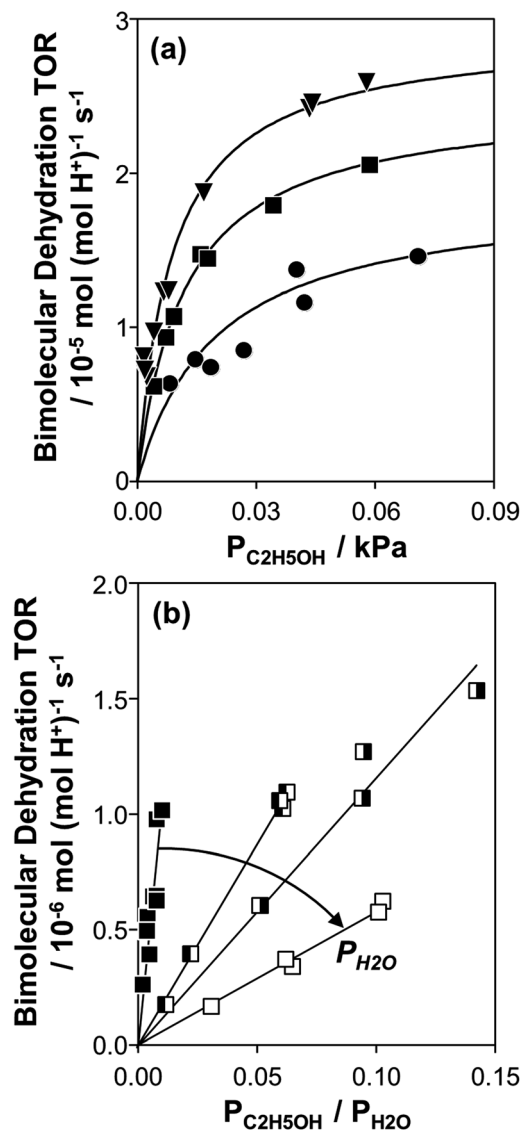
Fig. 1 (a) Bimolecular ethanol dehydration turnover rate (per H$^+$, 373 K) as a function of C$_2$H$_5$OH pressure, without co-fed H$_2$O, on H-Al-Beta-F(1.2) (●), H-Al-Beta-F(2.0) (■), and H-Al-Beta-OH(1.7) (▼). Solid lines represent regression to eqn (1). (b) Bimolecular ethanol dehydration turnover rate (per H$^+$, 373 K) on H-Al-Beta-F(2.0) as a function of the C$_2$H$_5$OH/H$_2$O pressure ratio, in the range 2–10 kPa H$_2$O (■), and at 40 kPa H$_2$O (◧), 50 kPa H$_2$O (◨), and 75 kPa H$_2$O (□).

H-Al-Beta zeolites with varying H$^+$ density (0.16–2.0 u.c.$^{-1}$), quantified during ethanol dehydration catalysis by *in situ* poisoning with 2,6-di-*tert*-butylpyridine (DTBP) to enable accurate normalization of turnover rates[79,80] (Fig. S4–S10, ESI†). Kinetic data in the absence of co-fed water serve to benchmark[81] experimental measurements to prior literature reports and set the stage for detailed investigations of the effects of water under conditions that approach capillary condensation and catalysis within liquid-like phases confined within microporous environments. In the absence of co-fed water, turnover rates increase linearly with ethanol pressure (<0.01 kPa) and approach constant values at higher ethanol

pressures (∼0.05 kPa, Fig. 1a). This functional dependence is consistent with an associative mechanism for bimolecular ethanol dehydration to DEE[82–85] (Fig. S11,† with further discussion in Sections S.2.4–S.2.5, ESI†), in which H$^+$ sites are occupied by MARI consisting of hydrogen-bonded ethanol monomers and protonated ethanol–ethanol dimers that are in quasi-equilibrium with gaseous ethanol; protonated dimers subsequently rearrange to form co-adsorbed DEE and water in the kinetically relevant step followed by product desorption in kinetically irrelevant steps to complete the catalytic cycle. These mechanistic assumptions lead to a rate expression for the bimolecular dehydration turnover rate that captures the measured dependence on ethanol pressure:

$$\frac{r_{DEE}}{[H^+]} = \frac{k_3 K_2 P_{C_2H_5OH}}{1 + K_2 P_{C_2H_5OH}} \tag{1}$$

where K_2 is the equilibrium constant to form the protonated ethanol–ethanol dimer from the hydrogen-bonded ethanol monomer and gaseous ethanol (kPa^{-1}), k_3 is the intrinsic bimolecular dehydration rate constant (mol (mol H$^+$) s^{-1}), and $P_{C_2H_5OH}$ is the ethanol pressure (kPa). The k_3 and K_2 values that result from this analysis (Table S1, ESI†) are similar within a factor of ∼2 and do not depend systematically on H$^+$ density among three H-Al-Beta samples (Fig. S13, ESI†), consistent with single-site catalytic behavior at H$^+$ sites and indicating that measured rates are not corrupted by transport phenomena according to the Madon–Boudart criterion.[86] These k_3 values further serve to benchmark our measurements against those in the literature[84] (details in Section S.2.1, ESI†).

Bimolecular dehydration turnover rates (373 K, per H$^+$) measured on H-Al-Beta-F(2.0) in the presence of co-fed water (2–75 kPa H$_2$O) are presented in Fig. 1b as a function of the ethanol/water pressure ratio. The inhibitory effects of water are consistent with the formation of an ethanol–water dimer species invoked previously to account for inhibition of mono-molecular 2-butanol dehydration rates by water on Brønsted acidic polyoxometalate clusters[56] (343 K, <0.5 kPa H$_2$O). Including the ethanol–water dimer as a candidate MARI alongside ethanol monomer and ethanol–ethanol dimer species leads to a modified rate expression:

$$\frac{r_{DEE}}{[H^+]} = \frac{k_3 K_2 P_{C_2H_5OH}}{1 + K_2 P_{C_2H_5OH} + K_4 P_{H_2O}} \tag{2}$$

where K_4 is the equilibrium constant to form the ethanol–water dimer from a hydrogen-bonded ethanol monomer and a gaseous water molecule (kPa^{-1}), and P_{H_2O} is the water pressure (kPa). The functional form of eqn (2) shows that an appreciable coverage of ethanol–ethanol dimers would lead to measured rates with fractional reaction orders in ethanol. The data in Fig. 1b are restricted to kinetic regimes where rates were strictly first-order in ethanol, which require that the coverage of ethanol–ethanol dimers at H$^+$ sites is negligible, as occurs in the limiting case where ethanol pressures are sufficiently low relative to co-fed water pressures ($P_{C_2H_5OH}/P_{H_2O}$ < 0.15):

$$\frac{r_{DEE}}{[H^+]} = \frac{k_3 K_2 P_{C_2H_5OH}}{1 + K_4 P_{H_2O}} \tag{3}$$

In the limiting case of excess water pressures, ethanol–water dimers are the sole MARI and rates depend linearly on the ethanol-to-water pressure ratio:

$$\frac{r_{DEE}}{[H^+]} = \frac{k_3 K_2}{K_4} \frac{P_{C_2H_5OH}}{P_{H_2O}} \quad (4)$$

At moderate water pressures (2–10 kPa, filled data points in Fig. 1b), eqn (4) accurately predicts the inhibitory effects of water, which reflects the requirement to displace water with ethanol in precursor complexes en route to the bimolecular dehydration transition state. The bimolecular dehydration turnover rate (373 K, per H⁺) is a single-valued function of ethanol/water pressure ratio in the range of 2–10 kPa of water ($P_{C_2H_5OH}/P_{H_2O}$ = 0.002–0.01, solid data points in Fig. 1b), consistent with full coverage of H⁺ sites by ethanol–water dimers. DFT calculations of water-assisted associative pathways (Fig. S64, ESI†) indicate that water co-adsorbs with an ethanol monomer to form an ethanol–water dimer (+5 kJ mol⁻¹; Fig. S64, ESI†), and a gas-phase ethanol subsequently adsorbs to form an ethanol–ethanol–water trimer (+24 kJ mol⁻¹, Fig. S64, ESI†), which can form DEE via an S_N2 transition state analogous to that formed when water is absent. The additional water molecule in the ethanol–ethanol–water trimer, however, acts as a proton shuttle between the framework and the H₂O leaving group, allowing the transition state to reside more distant from the framework $[AlO_{4/2}]^-$ and gain additional stabilization through dispersive interactions with the surrounding framework (Fig. S64, ESI†). Thus, apparent activation free energies for water-free and water-assisted associative pathways are comparable (Fig. S64, ESI†), indicating that as H⁺ become covered by $(C_2H_5OH)(H^+)(H_2O)_n$ MARI species, their corresponding transition states containing co-adsorbed H₂O become kinetically relevant (Section S.2.4, ESI†). These findings also indicate that mechanistic interpretation of the inhibitory effects of H₂O with varying water coverage requires more precise descriptions of the $(C_2H_5OH)(H^+)(H_2O)_n$ intermediates of different molecularity that can form DEE without complete desorption of H₂O, as we discuss below (Section 2.5).

At water pressures above 10 kPa (partially filled and unfilled data points in Fig. 1b), measured rates deviate from the single-valued function observed between 2–10 kPa and described by eqn (4), but remain first-order in ethanol pressure, according to the empirical relation:

$$\frac{r_{DEE}}{[H^+]} = k_{first} P_{C_2H_5OH} \quad (5)$$

where k_{first} is the apparent first-order rate constant in ethanol pressure (mol (mol H⁺)⁻¹ (kPa C₂H₅OH)⁻¹ s⁻¹), and can be quantified when $P_{C_2H_5OH}/P_{H_2O}$ < 0.15. The value of k_{first} in the form of eqn (5) also contains an unknown functional dependence on water pressure that is not described by eqn (4), because turnover rates decrease systematically with water pressure in higher pressure regimes (>10 kPa H₂O, Fig. 1b) at the same ethanol-to-water pressure ratio, indicating that water

inhibits turnover rates more strongly than the inverse order predicted by kinetic models where active sites are saturated with ethanol–water dimers (eqn (4)). The value of k_{first} was quantified as a function of water pressure (0.02–75 kPa, rate data in Fig. S15, ESI†) to include regimes corresponding to partial and full coverage by ethanol–water dimers (~0.02–10 kPa, described by eqn (3)) and the departure from the behavior described by eqn (4) (10–75 kPa), as shown in Fig. 2a. Combining eqn (3) and (5) gives an expression for k_{first} as a function of water pressure in regimes that include ethanol monomers and ethanol–water dimers as the MARI:

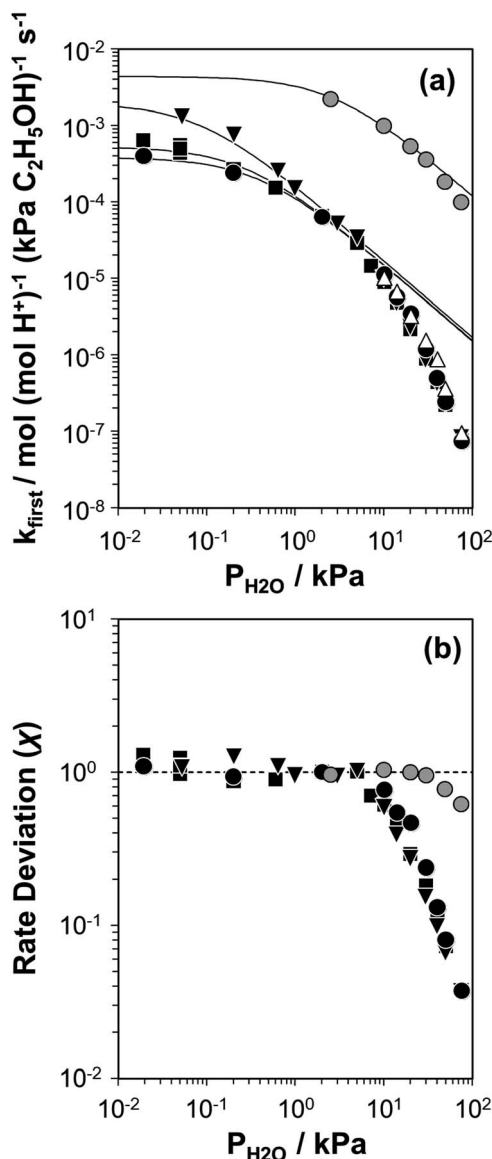$$\frac{r_{DEE}}{[H^+]P_{C_2H_5OH}} = \frac{k_3 K_2}{1 + K_4 P_{H_2O}} = k_{first} \quad (6)$$

Fig. 2 (a) Apparent first-order bimolecular ethanol dehydration rate constant (per H⁺, 373 K) and (b) rate deviation (χ) from the functional dependence of eqn (6), as a function of H₂O pressure on H-Al-Beta-F(0.16) (△), H-Al-Beta-F(1.2) (●, ● at 423 K), H-Al-Beta-F(2.0) (■), and H-Al-Beta-OH(1.7) (▼). Solid lines reflect regression to eqn (6).

The solid lines in Fig. 2a represent regression of k_{first} values (~0.02–10 kPa H_2O) to eqn (6), and give values for the lumped rate and equilibrium constant groups k_3K_2 and $k_3K_2K_4^{-1}$ in the low and high water pressure limits, respectively (Table S2, ESI†). The value of k_3K_2 reflects the free energy of the confined bimolecular dehydration transition state relative to the free energy of the confined ethanol monomer and gas-phase ethanol, and $k_3K_2K_4^{-1}$ reflects that of the confined transition state and gas-phase water relative to the confined ethanol–water dimer and gas-phase ethanol (additional discussion and derivations in Section S.2.6, ESI†). Values of $k_3K_2K_4^{-1}$ are essentially identical among the three H-Al-Beta samples (1.5–1.7 × 10^{-4} mol (mol H^+)$^{-1}$ s^{-1}, Table S2, ESI†), indicating that once H^+ are saturated with ethanol–water dimer intermediates, the free energy difference required to replace adsorbed water with adsorbed ethanol at the transition state is insensitive to differences in Si–OH density or other sample heterogeneities.

The deviation of k_{first} values from those predicted by eqn (6) at water pressures above ~10 kPa (Fig. 2a) was quantified as a function of water pressure up to 75 kPa. This deviation can be expressed as a function of water pressure by combining eqn (5) and (6):

$$\chi = k_{first}\left[\frac{k_3K_2}{1 + K_4P_{H_2O}}\right]^{-1} \qquad (7)$$

where values of k_3K_2 and K_4 are those estimated from rate data measured below 10 kPa H_2O corresponding to conditions in which eqn (3) holds. By definition, values of χ are unity in regimes where rate expressions involving ethanol monomers and ethanol–water dimers are MARI (~0.02–10 kPa H_2O, eqn (6)). The value of χ (Fig. 2b) deviates sharply from values of unity at high water pressures (>10 kPa) and systematically decreases with increasing water pressure to reach values <0.1 at and above 50 kPa H_2O; that is, measured turnover rates are more than one order of magnitude lower than predicted by eqn (6) under these conditions. Prior to mechanistic interpretation of this phenomenon, the possibility that values of χ below unity reflect the onset of intracrystalline mass transport limitations or a decrease in the number of active sites must be ruled out. Measured k_{first} values are insensitive to the density of H^+ sites within Beta zeolites at high H_2O pressures (0.2–2.0 H^+ u.c.$^{-1}$, Fig. S19, ESI†), consistent with the absence of transport corruptions according to the Madon–Boudart criterion;[86] the Mears criterion[87] also estimates that ethanol diffusion rates are orders of magnitude faster than measured reaction rates (Section S.2.3, ESI†). The number of catalytically active protons also does not decrease with increasing H_2O pressure, confirmed by quantifying the H^+ density at 30 kPa H_2O by in situ 2,6-di-tert-butylpyridine titration (0.66 H^+/Al, Fig. S5, ESI†) on H-Al-Beta-F(2.0), which was similar to that quantified at 1 kPa of H_2O (0.54 H^+/Al, Table 1). Thus, the dependence of χ on H_2O pressure is mechanistic in origin and may reflect differences in the MARI, the kinetically relevant steps, or solvation of adsorbed intermediates and transition states.

Values of k_{first} at 423 K on H-Al-Beta-F(2.0) (Fig. 2) are accurately described by eqn (6) between 2.5–30 kPa H_2O and are −1

order in water above 20 kPa H_2O (eqn (4)), in contrast to values of k_{first} at 373 K that are −1 order in water above 2 kPa H_2O. The delayed onset of the inverse water order kinetic regime to higher H_2O pressures at 423 K is consistent with lower coverages of inhibitory ethanol–water dimer intermediates at higher temperature, and is reflected by a lower K_4 value at 423 K (0.35, Table S3, ESI†) than at 373 K (2.5, Table S3, ESI†). In addition, χ values quantified at 423 K deviate from unity only above 30 kPa of H_2O, whereas χ values deviate from unity above 10 kPa H_2O at 373 K. The onset of sub-unity deviations in χ values becomes shifted to higher H_2O pressures at higher temperatures, similar to the later saturation of the surface by ethanol–water dimers when the kinetic regime is −1 order in water. By analogy, it is hypothesized that the dependence of χ on H_2O pressure is related to increasing coverages of water within micropores. Thus, we next probe the structures of adsorbed water and reaction intermediates in regimes approaching capillary condensation within micropores.

2.2. Characterization of intracrystalline water structures

The coverages and structures of H_2O prevalent during ethanol dehydration catalysis at 373 K were assessed using a combination of volumetric adsorption isotherms and in situ IR spectroscopy. The individual contributions of polar hydroxyl groups associated with both Brønsted acid sites (H^+) and Si–OH nests were systematically varied using the suite of H-Al-Beta-F samples that contain varying densities of H^+ u.c.$^{-1}$ (0.11–2.0, Table 1) and minimal densities of intracrystalline Si–OH defects (0.3–0.6 Si–OH u.c.$^{-1}$, quantified by CD_3CN IR on Ti-Beta-F zeolites[34]) because they were prepared in fluoride media.[77] Complete dealumination yielded deAl-Beta-F samples that contained Si–OH nest densities approximately equal to the number of H^+ u.c.$^{-1}$ before dealumination (Fig. S38†).
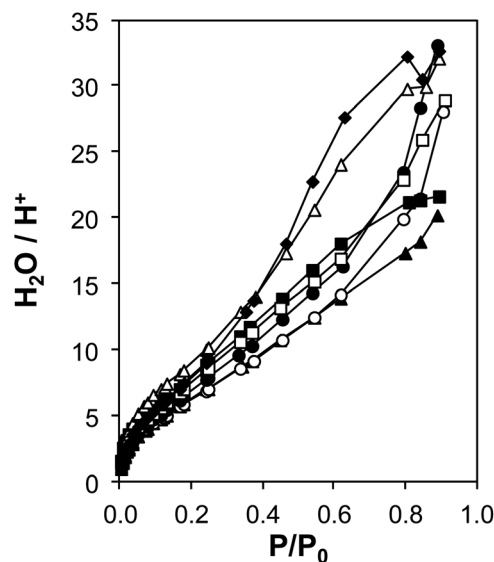

Fig. 3 Volumetric H_2O adsorption isotherms (293 K) on H-Al-Beta-F samples, with H^+ u.c.$^{-1}$ = 0.11 (◆), 0.16 (△), 0.57 (▲), 0.78 (○), 1.2 (●), 1.4 (□), 2.0 (■), after subtraction of the Si-Beta-F isotherm and normalizing by H^+ (raw isotherms are in Fig. S31, ESI†).
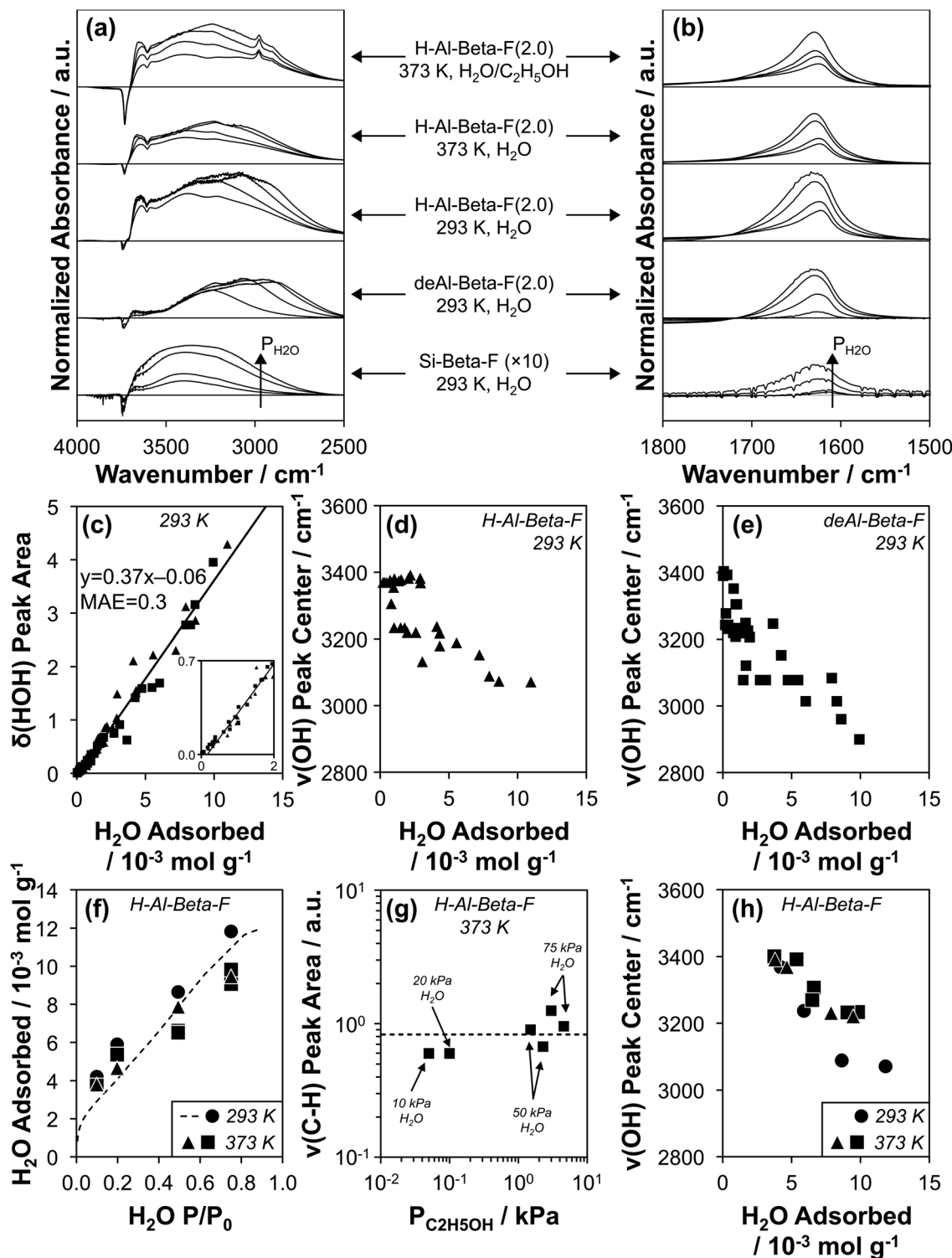
Fig. 4 (a and b) Baseline-corrected, normalized difference IR spectra of H_2O adsorbed on Si-Beta-F ($\times 10$ for clarity), deAl-Beta-F(2.0), and H-Al-Beta-F(2.0) at 293 K, of H_2O adsorbed on H-Al-Beta-F(2.0) at 373 K at H_2O P/P_0 values of 0.1, 0.2, 0.5, and 0.75, and of H_2O adsorbed on H-Al-Beta-F(2.0) with co-fed C_2H_5OH ($C_2H_5OH/H_2O = 0.005$ (10, 20 kPa H_2O) and 0.03 (50, 75 kPa H_2O)), in (a) the ν(OH) stretching region and (b) the δ(HOH) scissoring region. (c) Correlation of δ(HOH) area quantified from subtracted spectra at 293 K on all H-Al-Beta-F (▲) and siliceous Beta samples (deAl-Beta-F, Si-Beta-F, ■) listed in Table 1 with the amount of H_2O adsorbed at the same P/P_0 in volumetric adsorption isotherms (Fig. 3 and S32, ESI†). Solid line reflects line-of-best-fit. (d and e) Correlation of the ν(OH) peak center with the amount of H_2O adsorbed on (d) H-Al-Beta-F (▲) and (e) siliceous Beta samples (deAl-Beta-F, Si-Beta-F, ■). (f) Amount of H_2O adsorbed on H-Al-Beta-F(2.0) determined from δ(HOH) scissoring areas and the correlation in (c) at 293 K (●), 373 K (▲), and 373 K with co-fed C_2H_5OH (■). Dashed function corresponds to the volumetric adsorption isotherm of H_2O at 293 K (Fig. 3). (g) Variation in ν(CH) peak area with C_2H_5OH pressure on H-Al-Beta-F(2.0) at 373 K with co-fed H_2O at 10, 20, 50, and 75 kPa. Dashed line represents the average value. (h) Correlation of the ν(OH) peak center with the amount of H_2O adsorbed on H-Al-Beta-F(2.0) at 293 K (●), 373 K (▲), and 373 K with co-fed C_2H_5OH (0.05–4.6 kPa) (■).

Measured volumetric water adsorption isotherms (293 K, Fig. S31–S32a, ESI†) indicate that the adsorbed amount of water systematically increases with the density of hydrophilic groups on H-Al-Beta-F (H^+) or deAl-Beta-F (Si–OH), consistent with prior reports.[44,88] The isotherm measured on Si-Beta-F was subtracted from those of H-Al-Beta-F and deAl-Beta-F to obtain isotherms that predominantly reflect H_2O adsorption at their intra-crystalline hydrophilic binding sites (H^+, Si–OH nest),[44] and these isotherms were then normalized by the densities of H^+ or Si–OH nests to interrogate whether adsorption at individual functional groups is influenced by their density within crystallites.

H^+-normalized H_2O adsorption isotherms (Fig. 3) are invariant across the full range of H^+ densities (0.11–2.0 u.c.$^{-1}$) in H-Al-Beta-F zeolites at low relative pressures ($P/P_0 < \sim$0.2, 293 K), indicating that adsorption occurs preferentially at H^+ sites and generates $(H_3O^+)(H_2O)_n$ clusters of increasing size with increasing H_2O pressure. H^+-normalized isotherms deviate among samples at higher relative pressures ($P/P_0 > 0.2$), implying that $(H_3O^+)(H_2O)_n$ clusters have reached their maximum size and any additional H_2O that adsorbs instead is located within void spaces that are not occupied by $(H_3O^+)(H_2O)_n$ clusters, and at intracrystalline and extracrystalline Si–OH groups[45] that may be present in different amounts among samples. The saturation of $(H_3O^+)(H_2O)_n$ clusters at $P/P_0 \sim 0.2$ is also consistent with H_2O adsorption isotherms that are identical above $P/P_0 = 0.2$ on H-Al-Beta-F(0.57) and Na-Al-Beta-F(0.57), but offset by the difference in size of clusters stabilized by the different cations (Fig. S33, ESI†). At a P/P_0 value of 0.2, the average value of H_2O/H^+ is 7 ± 1 on H-Al-Beta-F samples with H^+ u.c.$^{-1}$ varying from 0.11–2.0 (Table S4, ESI†), similar to that reported previously.[44] The preferential adsorption of H_2O at H^+ and Si–OH nest defects was corroborated by volumetric adsorption isotherms and by determining isosteric heats of adsorption as a function of coverage from adsorption isotherms measured at different temperatures (details in Section S.2.7, ESI†). Measured isotherms provide a quantitative relationship between H_2O coverage and partial pressure that can be further related to the spectroscopic signatures of adsorbed H_2O structures present at different H_2O coverages.

Transmission IR spectra were collected on the suite of H-Al-Beta-F and deAl-Beta-F zeolites at 293 K exposed to H_2O pressures between 0.2–1.7 kPa ($P/P_0 = 0.1$–0.75). The spectrum of the zeolite before H_2O adsorption and that of gas-phase H_2O within the IR cell at the given P/P_0 value were subtracted from measured spectra (as illustrated in Fig. S39, ESI†) to provide difference spectra that reflect the vibrational signatures of adsorbed H_2O and of zeolite functional groups that are perturbed after adsorption. Representative spectra on Si-Beta-F, H–Al-Beta-F(2.0), and deAl-Beta-F(2.0) are shown in Fig. 4a and b (spectra on all samples in Fig. S40–S54, ESI†). Fig. 4b shows the peak centered between 1620–1630 cm^{-1} that corresponds to the δ(HOH) scissoring mode of adsorbed H_2O.[89] The position of the center of the δ(HOH) peak does not change significantly when H_2O adsorbs at different functional groups (H^+, Si–OH) or at different coverages, and its integrated area is proportional to the amount of water adsorbed at the same P/P_0 value quantified

by volumetric adsorption isotherms (Fig. 3). The linear relationship between quantity adsorbed and δ(HOH) peak area is shown in Fig. 4c and quantitatively predicts the amount adsorbed with a mean absolute error (MAE) of 0.3 mmol g^{-1} averaged among fifteen samples with H^+/Si–OH nests u.c.$^{-1}$ between 0–2.0, which enables measuring the amount of adsorbed H_2O on zeolite wafers directly from IR spectra instead of resorting to repeatedly estimating it from data collected at an equivalent external water chemical potential (T, P/P_0) in equilibrium with zeolite powders in separate volumetric adsorption isotherm measurements.

The O–H stretching region in Fig. 4a (2800–4000 cm^{-1}) includes negative peaks at 3735 cm^{-1} and 3745 cm^{-1} associated with the perturbation of isolated Si–OH groups within pores and at external crystallite surfaces, respectively,[90,91] a negative peak at 3600 cm^{-1} associated with the perturbation or disappearance of Brønsted acidic H^+ coordinated to the zeolite framework (ν(OH) of Al–OH)[90,92] in the case of H-Al-Beta-F(2.0), and a broad positive peak between $\sim$2800–3700 cm^{-1} that reflects a convolution of perturbed H^+/Si–OH groups and adsorbed H_2O molecules. The strong A, B, C triplet ($\sim$2900, $\sim$2400, and $\sim$1700 cm^{-1}) generated by Fermi resonance between the ν(OH), δ(HOH) and γ(OH) fundamentals of the Al–OH group in hydrogen-bonded 1 : 1 H_2O/H^+ complexes[93–96] is absent because all spectra are collected at higher coverages ($P/P_0 \geq 0.1$) after H^+ have been liberated from the framework as $(H_3O^+)(H_2O)_n$ clusters,[43] consistent with complete disappearance of the 3600 cm^{-1} peak at $P/P_0 = 0.1$ (Fig. S48b, ESI†).

The positive ν(OH) peak (Fig. 4a) is comprised of multiple components proposed to reflect O–H oscillators with increasing extents of hydrogen bonding as the wavenumber of the peak center decreases.[23,75,97] The peak between 3600–3700 cm^{-1} is reminiscent of a peak assigned to H_2O bound in one-dimensional chains within 0.8 nm diameter carbon nanotubes and to H_2O with non-hydrogen-bonded O–H groups pointing toward carbon nanotube walls in pores $\geq$1.4 nm in diameter (ν(OH) = 3640 cm^{-1}).[23] A similar peak has been assigned recently to the ν(OH) of H_2O (liquid) with one O–H group (3660 cm^{-1}) pointing toward a siloxane bridge on fused SiO_2 surfaces with 3.5–4.5 Si–OH nm^{-2} by vibrational sum frequency generation spectroscopy (vSFG).[98] These literature assignments are consistent with interpretation of this peak in Si-Beta-F and deAl-Beta-F (3600–3700 cm^{-1}) to reflect weakly correlated H_2O molecules that explore the full hydrophobic channel system, as we have identified previously in AIMD simulations of defect-free Si-Beta (1–3 H_2O u.c.$^{-1}$).[75] The ν(OH) peak at 3600–3700 cm^{-1} is present at higher intensity for H-Al-Beta-F(2.0) than for deAl-Beta-F(2.0) or Si-Beta-F, indicating that it is predominantly associated with non-hydrogen-bonded ("free") O–H groups of H_2O molecules that are part of $(H_3O^+)(H_2O)_6$ clusters, consistent with assignments made for free O–H groups (3700 cm^{-1}) at the interface between water and air by vSFG[99] and in gas-phase $Cs^+(H_2O)_{20}$ clusters by cryogenic photofragmentation mass spectrometry.[100] These assignments and spectral interpretations enable inferences into how the structure of water complexes and extended networks evolve
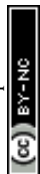
within confined spaces with increasing water pressure and coverage.

At low relative pressure ($P/P_0 = 0.1$), the dominant positive ν(OH) peak (Fig. 4a) is centered at 3390 cm^{-1} on Si-Beta-F, 3360–3380 cm^{-1} on H-Al-Beta-F zeolites (0.11–2.0 H$^+$ u.c.$^{-1}$), and 3220–3320 cm^{-1} on deAl-Beta-F zeolites (0.11–2.0 Si–OH nest u.c.$^{-1}$), and progressively shifts to lower wavenumbers as a function of coverage on both H-Al-Beta-F (Fig. 4d) and deAl-Beta-F (Fig. 4e). The ν(OH) peak on Si-Beta-F does not change its shape nor the position of its center significantly (within $\sim$40 cm^{-1}) with increasing coverage, and contains contributions from hydrogen-bonded Si–OH groups ($\sim$3400 cm^{-1})[101] and from the O–H oscillators of the H$_2$O molecules bound at them. Bound H$_2$O molecules lead to additional contributions that broaden the ν(OH) peak both above and below its center at $\sim$3400 cm^{-1}, and have been assigned to the hydrogen-bonded O–H group of water molecules in gas-phase Cs$^+$(H$_2$O)$_{20}$ clusters whose second O–H group is either hydrogen-bonded ($\sim$3410–3570 cm^{-1}) or free ($\sim$3080–3370 cm^{-1}), respectively.[100] Overtones of 2δ(HOH) $\sim$ 3200 cm^{-1} also contribute in this region.[100,102] The ν(OH) peak centered within a narrow range (3360–3380 cm^{-1}) at $P/P_0 = 0.1$ on H-Al-Beta-F samples (0.11–2.0 H$^+$ u.c.$^{-1}$) reflects predominantly (H$_3$O$^+$)(H$_2$O)$_n$ clusters of similar structure regardless of H$^+$ density ($n = 4$, Table S5, ESI†), and is broader than the ν(OH) peak on Si-Beta-F because of higher intensity in both the 3600–3700 cm^{-1} region (free O–H) and the $\sim$3080–3370 cm^{-1} region (hydrogen-bonded O–H in H$_2$O with free O–H), likely because the clustered structure of (H$_3$O$^+$)(H$_2$O)$_4$ leads to more free O–H groups than in the H$_2$O molecules hydrogen-bound at Si–OH groups in Si-Beta-F. The ν(OH) peak for H$_2$O adsorbed at Si–OH nests in deAl-Beta-F zeolites at $P/P_0 = 0.1$ (H$_2$O/Si–OH nest $= 5 \pm 2$, Table S6, ESI†) contains contributions from the aforementioned OH groups belonging to H$_2$O and perturbed Si–OH groups, but is centered at lower wavenumbers (3220–3320 cm^{-1}). The lower wavenumber and broader range of the peak center reflects contributions from clustered hydrogen-bonded H$_2$O molecules with free O–H groups at Si–OH nest defects, but not from perturbation among OH groups within Si–OH nests that were already hydrogen-bonded (to one another) prior to H$_2$O adsorption, in contrast to H$^+$ that are isolated and then become solvated as (H$_3$O$^+$)(H$_2$O)$_n$ after H$_2$O adsorption. Hydrogen-bonded clusters of H$_2$O molecules at Si–OH nests at lower coverages are consistent with AIMD simulations that show H$_2$O binding at the Si–OH nest at coverages between 1–5 H$_2$O per nest.[75]

As the coverage of H$_2$O increases at higher partial pressures ($P/P_0 = 0.2$–0.75), the ν(OH) peak centers on both H-Al-Beta-F and deAl-Beta-F zeolites decrease in wavenumbers (Fig. 4d and e) because additional H$_2$O primarily leads to increased peak area in the 2800–3200 cm^{-1} region (see peak centers of differential-subtracted spectra between $P/P_0 = 0.2$–0.75, Fig. S40b–S52b, ESI†). These peaks are not associated with ice-like water structures[103] despite their similar wavenumbers to that of ice (3200 cm^{-1}),[104] but instead have been shown to result from Fermi resonance between 2δ(HOH) modes and ν(OH) modes when H$_2$O molecules are coupled in extended hydrogen-

bonded networks.[102,105,106] As the extent of hydrogen-bonding increases, the ν(OH) mode shifts to lower wavenumber and the splitting caused by Fermi resonance results in an apparent decrease in intensity above 2δ(HOH) and an increase below it.[102,105,106] This O–H oscillator signal is made further diffuse by its coupling to the modes of the local extended hydrogen-bonded network.[107] Isotopic D$_2$O/HOD/H$_2$O mixtures that are dilute in H$_2$O were used previously to identify this phenomenon because the ν(OH) mode is not split by the 2δ(HOD) = 2900 cm^{-1} mode,[102] and has been verified here using a 16 : 8 : 1 D$_2$O : HOD : H$_2$O mixture[106] on Si-Beta-F and deAl-Beta-F(2.0), where the ν(OH) peak center does not shift to lower wavenumbers under the same coverage regimes (Fig. S55–S56, ESI†). Although increased ν(OH) intensity between 2800–3200 cm^{-1} does not quantitatively correspond to a particular species or structure, it does reflect the formation of extended hydrogen-bonded networks, as we have identified in AIMD simulations of Beta zeolites containing one Si–OH nest per unit cell.[75] These networks form in both H-Al-Beta-F and deAl-Beta-F zeolites at relative pressures of H$_2$O above $\sim$0.2, consistent with shifts in the ν(OH) peak center to lower wavenumbers with increasing coverage (Fig. 4d and e), and with adsorption isotherms on H-Al-Beta-F zeolites that are proportional to H$^+$ density up to $P/P_0 \sim$ 0.2 to generate (H$_3$O$^+$)(H$_2$O)$_6$ clusters before extended hydrogen-bonded networks form and surround these clusters. These (H$_3$O$^+$)(H$_2$O)$_6$ clusters remain intact as H$_2$O networks surround them, in contrast to H$_2$O clusters at Si–OH nests that restructure to integrate within these extended hydrogen-bonded networks as observed in our prior AIMD simulations (>5 H$_2$O u.c.$^{-1}$),[75] which is consistent with ν(OH) peak centers in IR spectra that represent the majority of H$_2$O molecules participating in extended networks and thus reach lower values in deAl-Beta-F zeolites (Fig. 4e) than in H-Al-Beta-F zeolites (Fig. 4d). Extended hydrogen-bonded H$_2$O networks within H-Al-Beta-F zeolites form in similar relative pressure regimes ($P/P_0 = 0.2$–0.75) to those where kinetically measured χ values deviate from unity, indicating that such networks are responsible for more severe H$_2$O inhibition; however, a mechanistic basis that validates the identity of the assumed reaction intermediates (cf. Fig. S11†) is required.

In situ IR spectra were collected at 373 K on H-Al-Beta-F(2.0) under conditions analogous to those of turnover rate measurements to verify the formation of extended hydrogen-bonded networks in the presence of C$_2$H$_5$OH at reaction temperature. H$_2$O was fed at pressures of 10–75 kPa ($P/P_0 = 0.1$–0.75) corresponding to the regime where χ values deviate from unity (Fig. 2b), and C$_2$H$_5$OH was additionally included at C$_2$H$_5$OH/H$_2$O ratios between 0.005–0.06 where k_{first} values were quantified on H-Al-Beta-F(2.0) (Fig. 1b). The shape and position of δ(HOH) peaks at 373 K and 293 K are similar (Fig. 4b), and their areas indicate that the coverage of H$_2$O (at 373 K) within micropores as quantified by the correlation in Fig. 4c is similar to that quantified by volumetric adsorption isotherms (at 293 K) in the same relative pressure regime ($P/P_0 = 0.1$–0.75, Fig. 4f). We note, in passing, that using the correlation in Fig. 4c assumes that the integrated molar extinction coefficient for δ(HOH) is invariant between 293–373 K. Values of H$_2$O coverage

were similar (within 20%) with and without co-fed C_2H_5OH (Table S8, ESI†), indicating that under these conditions (C_2H_5OH/H_2O = 0.005–0.06), C_2H_5OH does not significantly displace H_2O in the bulk adsorbed H_2O phase. Adsorbed C_2H_5OH can be identified in IR spectra by $\nu(C–H)$ peaks at 2905 and 2980 cm^{-1} (Fig. 4a). Similar $\nu(C–H)$ peak areas (within 2×, Fig. 4g) quantified over a wide range of C_2H_5OH pressures (0.05–4.6 kPa) are consistent with saturation of sites with ($C_2H_5OH)(H^+)(H_2O)_n$ MARI that give rise to apparent first-order kinetics in $P_{C_2H_5OH}$ (Fig. 1b). The $\nu(OH)$ region (Fig. 4a) shows similar increases in peak area (2800–3200 cm^{-1}, see also differential subtracted spectra in Fig. S57–S58, ESI†) corresponding to the formation of extended hydrogen-bonded H_2O networks between 10–75 kPa H_2O at 373 K both with and without co-fed C_2H_5OH, which is reflected in shifts in the $\nu(OH)$ peak center (Fig. 4h) from 3400 cm^{-1} (10 kPa H_2O) to 3220–3230 cm^{-1} (75 kPa H_2O).

In summary, volumetric adsorption isotherms and heats of adsorption of H_2O indicate that water adsorbs preferentially at low coverages at hydrophilic binding sites (H^+, Si–OH) within hydrophobic zeolite pores, then forms $(H_3O^+)(H_2O)_6$ clusters[44,45] (P/P_0 < 0.2) and extended hydrogen-bonded networks (P/P_0 > 0.2). *In situ* IR spectra measured at 373 K under conditions corresponding to those where χ values deviate from unity (>10 kPa H_2O) reveal concomitant formation of extended hydrogen-bonded H_2O structures that solvate clustered ($C_2H_5OH)(H^+)(H_2O)_n$ MARI at active sites within H-Al-Beta-F zeolites. The free energies of these intermediates and putative transition states are next interrogated by AIMD and metadynamics, respectively. AIMD simulations were performed to sample the many possible configurations that these water–ethanol clusters can adopt under reaction conditions. While one additional water may act as a proton shuttle at the transition state (Section 2.1), the participation of larger $(H_2O)_n$ clusters in ethanol dehydration transition states may introduce qualitatively different behavior that can be explored using metadynamics simulations.

2.3. *Ab initio* molecular dynamics of water–ethanol mixtures

AIMD simulations were performed at 373 K with H_2O in H-Al-Beta (1 H^+ u.c.$^{-1}$) to determine the structure of the confined, protonated water network and compare with experimentally measured water coverages. Higher water coverages require AIMD simulations because the many potential adsorbate configurations are intractable to model using static DFT calculations. Our previous work on the structure and stability of water networks in Sn-Beta and deAl-Beta zeolites showed that locally stable water clusters form at coverages between 5–8 H_2O u.c.$^{-1}$ and that such clusters coexist with extended water networks at higher coverages.[75] Here, we used this coverage range (5–8 H_2O u.c.$^{-1}$) as a starting point to reduce the number of computationally demanding AIMD simulations required to find locally stable water cluster sizes, and we expect this will serve as an example of how the techniques developed in Bukowski *et al.*[75] can be practically applied. Shuttling of the H^+ among H_2O molecules in the cluster is facile, which requires
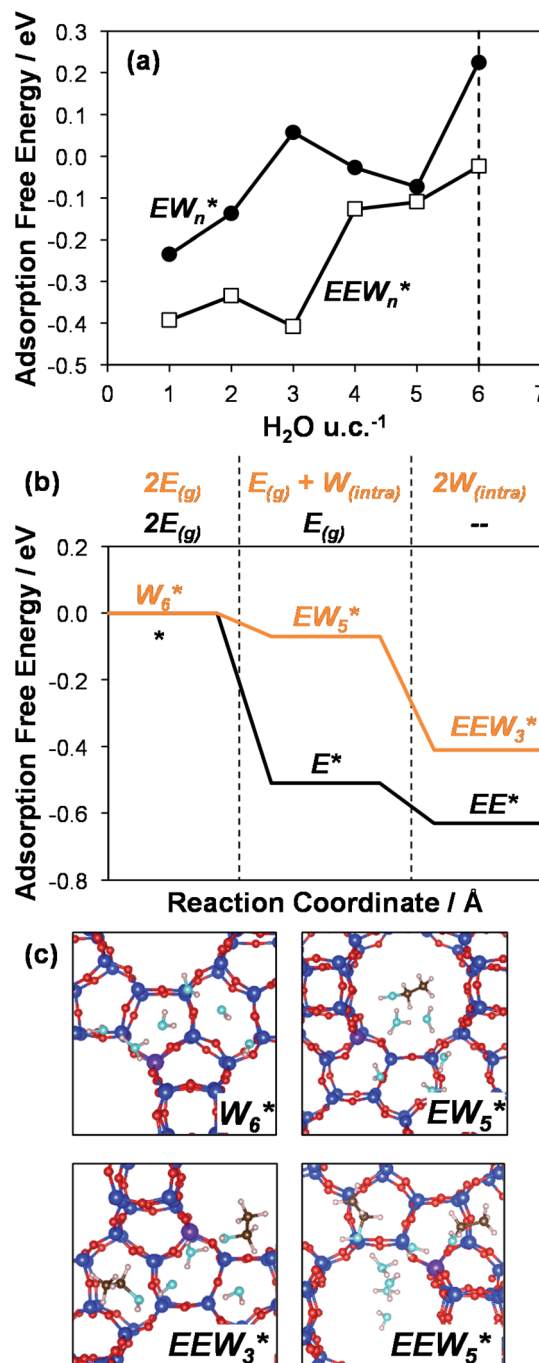
Fig. 5 (a) Gibbs free energies of adsorption (373 K) of ethanol monomer and dimer species with 1–6 co-adsorbed H_2O (n) calculated by AIMD, referenced to gas-phase ethanol molecules. Vertical dashed line indicates the locally stable pure-H_2O cluster size (W_6^*). (b) Gibbs free energy of adsorption (373 K) for ethanol monomer and dimer species at H_2O coverages corresponding to the local minima of (a) and compared to ethanol monomer and dimer adsorption in the gas phase. $W_{(intra)}$ refers to intrapore water at other pure H_2O clusters and is calculated from the intensive Gibbs free energy of water within the Beta pore. (c) Representative geometries of the stable water cluster (W_6^*), ethanol monomer cluster (EW_5^*), ethanol dimer cluster (EEW_3^*), and the ethanol–water dimer cluster formed by adsorption of one ethanol molecule at the stable monomer cluster (EEW_5^*).

special considerations for adsorbate entropy (detailed discussion in Section S.2.8, ESI†). A local free energy minimum was found at 6 H_2O u.c.$^{-1}$ (Fig. S69, ESI†), which corresponds to a $(H_3O^+)(H_2O)_5$ cluster (W_6^*, Fig. 5c). This stable cluster size is within error of that measured by experimental volumetric H_2O adsorption isotherms (7 ± 1 H_2O u.c.$^{-1}$) and is consistent with the cluster sizes identified in prior investigations of H-Al-MFI zeolites.[43–45]

In AIMD simulations, the H^+ is solvated within the H_2O cluster, consistent with the disappearance of ν(OH) stretches for Al–O(H)–Si groups in experimentally measured IR spectra (Fig. 4a). The fraction of time that H^+ is solvated as H_3O^+ rather than coordinated to the framework was evaluated by quantifying the distance of the closest H atom to a framework oxygen bound to Al in each frame of each trajectory. For the smallest water cluster size simulated (W_5^*), H^+ is solvated in the cluster for 66% of the 20 ps simulation (Fig. S68, ESI†), indicating that H^+ primarily, but not exclusively, resides within the solvated H_3O^+ cluster at 373 K. These AIMD simulations at 373 K reveal an equilibrium between solvated and framework H^+ states that depends on water coverage, in contrast to DFT calculations at 0 K indicating that a solvated H^+ is more stable than a framework H^+ for all water coverages greater than 1 H_2O/H^+. Thus, caution should be used in interpreting the location of H^+ from DFT calculations at 0 K, as AIMD simulations provide more rigorous assessment of the solvation environment of H^+ at reaction conditions. These simulations in the absence of reactant molecules (C_2H_5OH) successfully predict the structures of clustered $(H_3O^+)(H_2O)_n$ that have been previously studied,[43–45] and suggest that analogous AIMD simulations incorporating C_2H_5OH molecules can provide accurate insights into the structure sand dynamics of reactant-solvent complexes relevant for catalysis.

We next used AIMD to simulate $(C_2H_5OH)_m(H^+)(H_2O)_n$ clusters adsorbed in H-Al-Beta zeolites at 373 K, where n was varied between 1–6 and $m = 1, 2$, corresponding to ethanol monomer and ethanol–ethanol dimer species with different degrees of solvation by H_2O. The free energy of adsorption of these ethanol molecules was calculated from AIMD relative to gas-phase ethanol and the same number of H_2O molecules adsorbed within the zeolite:

$$\Delta G_{E_m,\text{ads}} = G_{E_m,\text{solv}} - mG_{E_{(g)}} - G_{W_n,\text{solv}} \quad (8)$$

where $G_{E_m,\text{solv}}$ is the total free energy of the system calculated by AIMD of the $(C_2H_5OH)_m(H^+)(H_2O)_n$ cluster, $G_{W_n,\text{solv}}$ is the total free energy of the system calculated by AIMD of the $(H^+)(H_2O)_n$ cluster, and $G_{E_{(g)}}$ is the free energy of gas-phase ethanol. The free energy of adsorption of gas-phase C_2H_5OH into $(C_2H_5OH)_m(H^+)(H_2O)_n$ clusters is shown as a function of the number of H_2O molecules (n) in Fig. 5a. In general, C_2H_5OH adsorption to form $(C_2H_5OH)_m(H^+)(H_2O)_n$ is less exergonic as the number of solvating H_2O molecules increases, because C_2H_5OH disrupts existing hydrogen bonds among H_2O molecules in clusters of increasing size. In the case of one C_2H_5OH molecule, a local minimum in free energy is observed at $(C_2H_5OH)(H^+)(H_2O)_5$, after which additional H_2O significantly increases the

adsorption free energy (by 0.3 eV). This indicates that the largest stable $(C_2H_5OH)(H^+)(H_2O)_n$ cluster occurs at $n = 5$ (EW_5^*, Fig. 5c), consistent with displacement of one H_2O molecule in the $(H^+)(H_2O)_6$ cluster by C_2H_5OH, which is found to be located near the H_3O^+ ion during the simulations. This $(C_2H_5-OH)(H^+)(H_2O)_5$ species is likely the MARI in experimentally measured kinetics and IR spectra (373 K), and it becomes increasingly solvated by extended hydrogen-bonded water networks that surround it in the water pressure regimes (10–75 kPa H_2O) where χ values deviate from unity, as detected by in situ IR spectra (Fig. 4). The local free energy minimum for $(C_2-H_5OH)_2(H^+)(H_2O)_n$ species occurs at $n = 3$, indicating that adsorption of an additional ethanol prior to reaction further disrupts the hydrogen-bonding network of the H_2O cluster; thus, at $n = 5$ (EEW_5^*, Fig. 5), both adsorbed ethanol molecules participate in hydrogen bonding with three clustered waters, but not the remaining water molecules in the cluster. Analogous disruption of extended water networks is therefore expected when they solvate bimolecular transition states at high water coverages.

The free energy of ethanol adsorption at water-solvated hydronium ions is compared to adsorption at protons without any solvent in Fig. 5b. Free energies of ethanol adsorption are referenced to the stable water cluster (W_6^*), where ethanol displaces one water from this cluster to form EW_5^* and a displaced intraporous water molecule in equilibrium with the most stable water cluster ($W_{(intra)}$). The free energy of ethanol adsorption is weaker by 0.44 eV in the presence of solvent because the water network must reorganize to form a stable ethanol–water cluster, and interactions with the proton are redistributed among the water molecules. Adsorption of a second ethanol further reduces the number of clustered water molecules (EEW_3^*), which releases two additional intraporous water molecules ($3W_{(intra)}$ total) and leads to a differential free energy of adsorption (-0.34 eV) that is more than twice that of the gas phase (-0.12 eV). This difference is primarily enthalpic in origin, as entropies of adsorption in the solvated and gas phases differ by only 10 J mol^{-1} K^{-1}, reflecting how the presence of confined water and its reorganization influence heats of adsorption of reactive intermediates.

The solvation of H^+ within $(C_2H_5OH)_m(H^+)(H_2O)_n$ was also compared with that in $(H^+)(H_2O)_n$ clusters, using the same criterion that any H^+ within 1.1 Å of a framework oxygen is considered to be coordinated to the zeolite framework (Fig. S68, ESI†). Whereas the protonated dimer was the most energetically stable configuration in 0 K DFT calculations, AIMD simulations show that at 373 K the proton remains bound to a framework site for 89% of the simulation time for the ethanol–water dimer ($m = 1$, $n = 1$). Both the framework-protonated state and solvated hydronium ion state of EW* are close in energy (~ 0.2 eV) in the 0 K DFT calculations, such that the free energy differences at 373 K likely reflect entropic effects on H^+ solvation. In the locally stable ethanol monomer cluster (EW_5^*), the proton remains solvated for >98% of the simulation time, indicating that larger water clusters more effectively solvate protons away from the zeolite framework. Two ethanol molecules are sufficient to solvate the H^+ away from the zeolite

framework without water,[108] and thus the H^+ remains solvated nearly 100% of the simulation time across the entire range of water coverages (n = 1–6 H_2O, m = 2). The H^+ remains solvated as H_3O^+ in $(C_2H_5OH)_2(H^+)(H_2O)_n$ species rather than being shared between the two C_2H_5OH in a protonated dimer, which we surmise leads to additional free energy penalties to reorganize positive charges and localize them at the ethyl group in S_N2 transition states that form diethyl ether and water, as investigated next.

2.4. *Ab initio* simulation of dehydration transition state solvation using metadynamics

The configurations of the bimolecular dehydration transition state in the presence of five H_2O molecules were explored further in metadynamics simulations. While EEW_3^* was identified as the most stable solvated ethanol dimer, a different number of solvent molecules may preferentially stabilize the dehydration transition state given different opportunities for available hydrogen-bonding configurations in H_2O that surround the transition state. A water phase diagram could be constructed for the transition state; however, this would require biased AIMD for every water cluster size. It is necessary to choose a reasonable number of waters to simulate a realistic solvating environment. If the chosen cluster size is larger than that present at equilibrium, water will phase separate to form the most stable cluster and gas-like water given sufficient simulation time, based on previous data for Lewis acids.[75] This indicates that an overestimate of the simulated cluster size is more rigorous than an underestimated cluster size, which would be unstable and prevented from phase separating to form a stable solvation shell. The $(C_2H_5OH)_2(H^+)(H_2O)_5$ intermediate was thus chosen as a reasonable upper bound for the solvated transition state, and the collective variables were chosen as the distances between the C_α atom of the ethanol bound to H_3O^+ and its O atom, which becomes the H_2O leaving group at the transition state, and the distance between this same C_α atom in the first ethanol and the O' atom of the second ethanol molecule, which is the nucleophilic O atom at the transition state. As such, at the initial state ((1), Fig. 6), the O–C_α bond distance is ~1 Å, while the O'–C_α distance explores a larger configurational space limited to ~2–3 Å by the hydrogen-bonding interaction between the two ethanol molecules. The opposite is true at the final state ((3), Fig. 6) once the O'–C_α bond has been fully formed in diethyl ether at a distance of ~1 Å, while the leaving group H_2O that determines the O–C_α distance may diffuse 2–5 Å away from the product DEE.

The metadynamics simulation was carried out for a total time of 175 ps and included 27 barrier re-crossings in the span of 5 ps. The 1-D projection of the minimum free energy path (Fig. 6b) between the reactant and product basins gives a forward barrier of 1.7 eV and a reverse barrier of 3.0 eV. These are larger than those values calculated by gas-phase DFT with one water molecule (0.8 eV and 1.2 eV, respectively), in part reflecting the biased metadynamics sampling of initial and product states with high configurational entropy due to the number of solvent molecules. The number of transition states sampled in the simulation (27
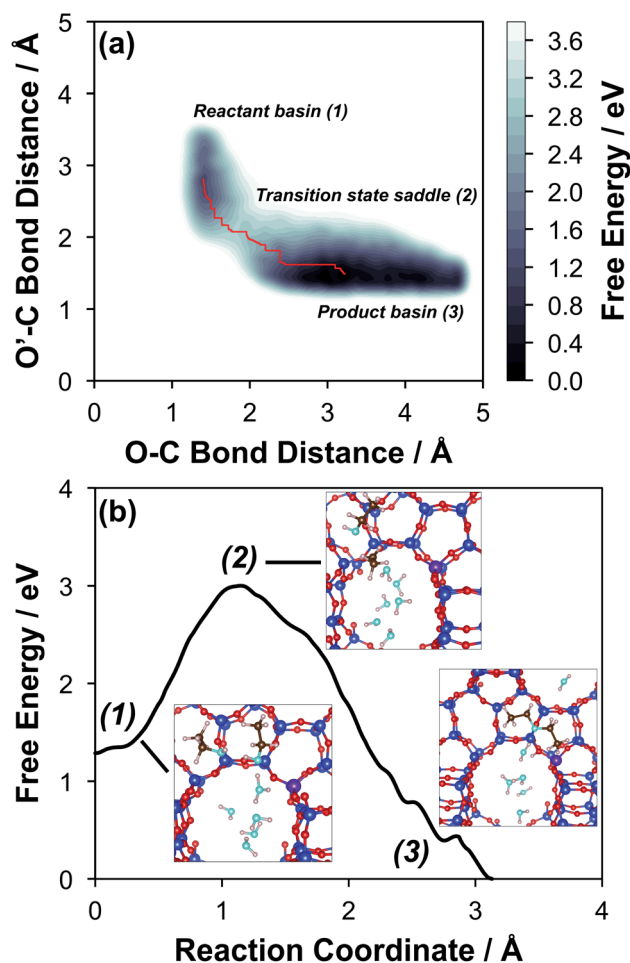

Fig. 6 (a) Free energy contour plot of diethyl ether formation with five co-adsorbed H_2O molecules calculated by metadynamics with collective variables of the O–C_α bond distance of one ethanol molecule, and the O'–C_α bond distance of carbon from the first ethanol and oxygen of the second ethanol. The minimum energy path connecting the reactant and product basins is indicated in red. (b) The minimum energy plot obtained by projecting the minimum energy path from (a) into a 1-D reaction coordinate. Numbering reflects the same basins and saddle point as (a). Representative geometries of species in the reactant basin, transition state saddle, and product basin are included in the plot area.

barrier re-crossings) may not reflect the full relative number of microstates available to the system at the transition state *versus* the reactant and product basins. This is not uncommon for MD sampling techniques, and once the saddle point is identified, umbrella sampling can be used to refine the reaction barriers with biasing potentials along the reaction coordinate.[109] Umbrella sampling is, however, unfeasible in an AIMD simulation this large in scale. An additional 18 ps AIMD simulation with O–C_α–O bonds constrained to the metadynamics saddle point was therefore used to improve sampling of the solvated transition state. The apparent activation energy referenced to the EW_5^* MASI was 1.3 eV, which is reasonable in comparison to the gas-phase energetics.

Metadynamics saddle points also provide physical insight into how solvent molecules structure at the transition state. A representative transition state from metadynamics ((2), Fig. 6)

resembles the S_N2 configurations of DEE-formation transition states calculated with zero or one co-adsorbed H_2O molecule, respectively (Fig. S64, ESI†). The O–C and O′-C distances are approximately equivalent, where the $C_2H_5^+$ group lies equidistant between the nucleophilic C_2H_5OH and the leaving group H_2O. Here, charge has transferred from H_3O^+ to the $C_2H_5^+$ group, and thus five H_2O molecules solvate the transition state,

rather than the four that solvate the $(C_2H_5OH)_2H_3O^+$ precursor complex. The requirement to dissociate this bound H_2O molecule from the H^+ active site en route to the bimolecular dehydration transition state results in the limiting case of a −1 reaction order in H_2O. In contrast to transition states with zero or one co-adsorbed H_2O (Fig. S64, ESI†), transition state (2) in Fig. 6 is stabilized distant from the framework Al atom because
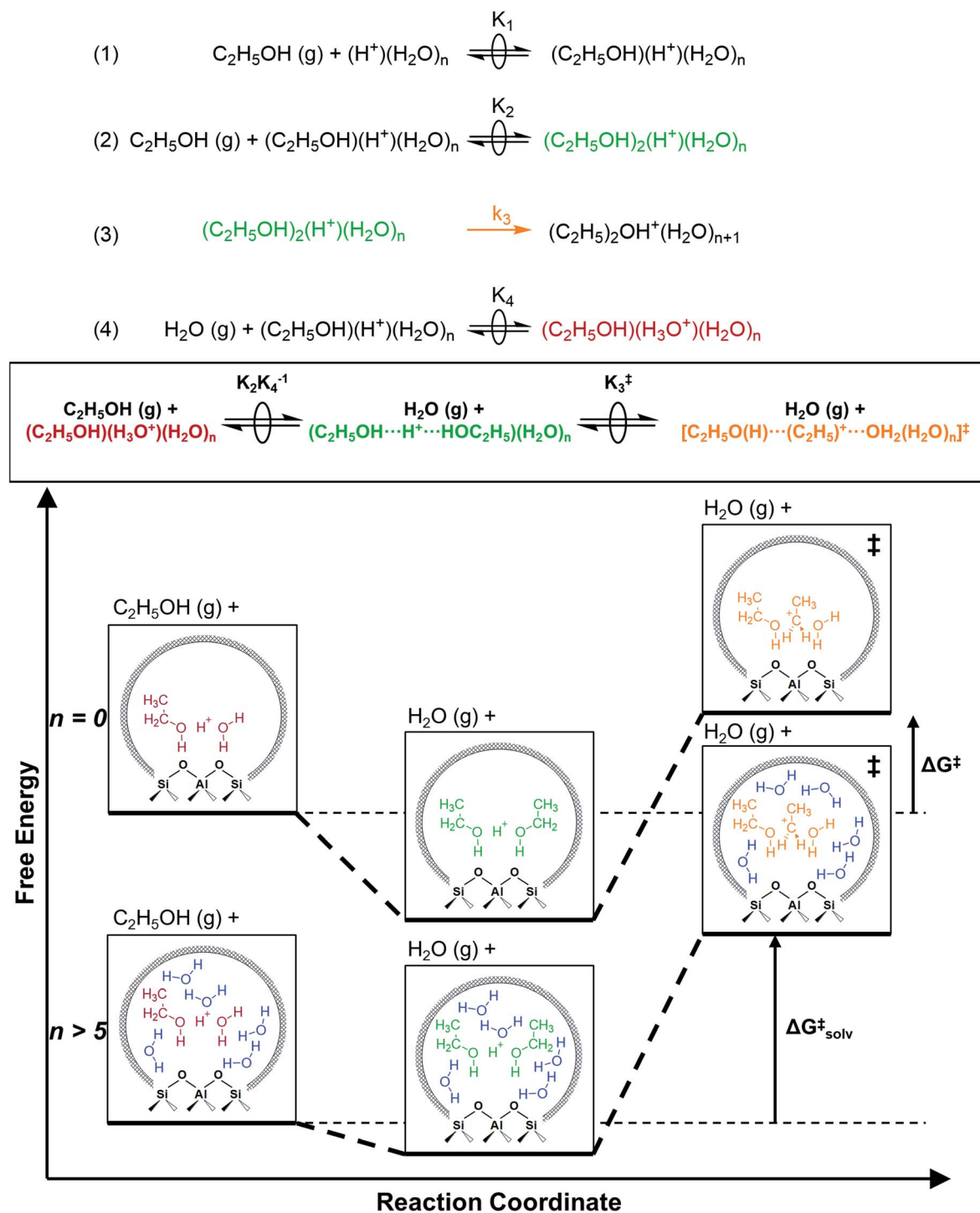
Scheme 1 Series of elementary steps for ethanol dehydration catalyzed by solvated hydronium ions, and free energy diagram illustrating the effects of solvation by extended hydrogen-bonded H_2O networks.
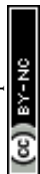
of the delocalization of the H^+ charge as H_3O^+ in its precursor state. This enables the transition state to effectively maximize its van der Waals contacts with the surrounding pore environment compared to when it is electrostatically constrained near the framework Al. The transition state and adsorbed precursors reside on the periphery of the H_2O cluster rather than within it, indicating that under this coverage regime (up to 5 H_2O per H^+), the primary function of H_2O is to solvate the H^+ active site as $(H_3O^+)(H_2O)_n$. The location of the transition state on the periphery of the H_2O cluster is consistent with kinetically relevant formation of DEE catalyzed by H_3O^+ through transition states that do not require a reduction in the size of H_2O clusters.

In summary, these combined theoretical simulations indicate that the structure of $(C_2H_5OH)(H^+)(H_2O)_n$ MARI are analogous to those of $(H^+)(H_2O)_n$, where one C_2H_5OH molecule displaces one H_2O molecule, and that these MARI may access kinetically relevant DEE formation transition states after adsorption of a second ethanol and displacement of one H_2O molecule from the H^+ active site. At coverages up to 5 H_2O/H^+, prior to the formation of extended hydrogen-bonded H_2O networks, C_2H_5OH molecules interact minimally with clustered H_2O and prefer to react at the periphery of such clusters within zeolite voids.

2.5.   Mechanistic implications of solvation by condensed water structures

The similarity of diethyl ether transition state free energies, regardless of the number of H_2O molecules in $(C_2H_5\text{-}OH)(H^+)(H_2O)_n$ MARI, is consistent with the elementary steps to form DEE in Fig. S11,† but with the additional complexity that increasing solvation of H^+ by H_2O leads to new configurations of $(C_2H_5OH)(H_3O^+)(H_2O)_{1-5}$ as MARI rather than only $(C_2H_5OH)(H^+)(H_2O)$ species, as shown in Scheme 1. When $n = 0$, the elementary steps in Scheme 1 are identical to those in Fig. S11,† so that addition of H_2O to form $(H_3O^+)(H_2O)_n$ does not impact the functional form of the rate expressions. Clustered $(C_2H_5OH)(H_3O^+)(H_2O)_{1-5}$ MARI must desorb one H_2O molecule en route to transition states that localize positive charge at the ethyl group, recovering the -1 reaction order in H_2O as the limiting case when surfaces are saturated by $(C_2H_5OH)(H_3O^+)$ $(H_2O)_{4-5}$ MARI (5 predicted by experiments, 4 by theory). Beyond the maximum cluster size, as shown by *in situ* IR spectra (293 and 373 K), additional adsorbed water begins to form extended hydrogen-bonded networks that solvate the MARI, which corresponds to kinetic regimes where χ values deviate from unity. Rate expressions derived from steps 1–4 in Scheme 1 that take this solvation into account, given that eqn (3) does not, are therefore required to provide a mechanistic basis for the stronger inhibition by H_2O when extended water networks are formed. Within the formalism of transition state theory,[110] $(C_2H_5OH)(H_3O^+)(H_2O)_n$ MARI and gas-phase C_2H_5OH (*i.e.*, the apparent initial state) are considered to be in equilibrium with $[C_2H_5O(H)\cdots(C_2H_5)^+\cdots OH_2(H_2O)_n]^‡$ and gas-phase H_2O (*i.e.*, the apparent final state):

$$\frac{r_{\text{DEE}}}{[H^+]} = \frac{k_B T}{h} C_‡ \Big/ [H^+] \tag{9}$$

where k_B is Boltzmann's constant, T is the temperature, h is Planck's constant, and $C_‡$ is the concentration[111] of the transition state, whose concentration can be expressed through $K^‡$, the transition state equilibrium constant:

$$K^‡ = \frac{a_‡ a_{H_2O(g)}}{a_{EW_n} a_{C_2H_5OH(g)}} \tag{10}$$

where a_i is the thermodynamic activity of species i. Replacing activities with activity coefficients and concentrations ($a_i = \gamma_i C_i$) in eqn (10), solving for $C_‡$, and substituting into eqn (9) gives:

$$\frac{r_{\text{DEE}}}{[H^+]} = \frac{k_B T}{h} K^‡ \frac{\gamma_{EW_n}}{\gamma_‡} \frac{\gamma_{C_2H_5OH(g)}}{\gamma_{H_2O(g)}} \frac{C_{C_2H_5OH(g)}}{C_{H_2O(g)}} \frac{C_{EW_n}}{[H^+]} \tag{11}$$

Eqn (11) can be simplified further by restricting its use to the conditions where experimental kinetics were collected with $(C_2H_5OH)(H_3O^+)(H_2O)_n$ as the sole MARI (373 K, 2×10^{-3} to 10 kPa C_2H_5OH, 0–75 kPa H_2O), under which $C_{EW_n}/[H^+] = 1$ because of the MARI assumption, and $\gamma_{C_2H_5OH(g)}/\gamma_{H_2O(g)} = 1$ because the gas-phase activity coefficients of both C_2H_5OH and H_2O are nearly unity under these conditions, which are far from their critical temperatures and pressures (H_2O $P_c = 22$ MPa, $T_c = 647$ K; C_2H_5OH $P_c = 6.4$ MPa, $T_c = 516$ K).[112] Assumption of an ideal gas phase also allows converting the ratio of concentrations to one of pressures to arrive at an expression for the bimolecular ethanol dehydration turnover rate that is similar to eqn (4):

$$\frac{r_{\text{DEE}}}{[H^+]} = \frac{k_B T}{h} K^‡ \frac{\gamma_{EW_n}}{\gamma_‡} \frac{P_{C_2H_5OH}}{P_{H_2O}} \tag{12}$$

Upon relating the transition state equilibrium constant to those of elementary steps in Scheme 1 (full derivation in Section S.2.9, ESI†):

$$\frac{r_{\text{DEE}}}{[H^+]} = \frac{k_3 K_2}{K_4} \frac{\gamma_{EW_n}}{\gamma_‡} \frac{P_{C_2H_5OH}}{P_{H_2O}} \tag{13}$$

it is evident that under conditions where solvation of both the MARI and transition state are thermodynamically ideal (or more generally under any conditions where their activity coefficients fortuitously cancel[113]), eqn (13) is identical to eqn (4). It therefore follows that:

$$\chi = \frac{\gamma_{EW_n}}{\gamma_‡} \tag{14}$$

which provides a mechanistic basis to interpret deviations in χ values below unity at increasing water pressures.

As extended hydrogen-bonded H_2O networks form and solvate $(C_2H_5OH)(H_3O^+)(H_2O)_{4-5}$ MARI and transition states, the activity coefficient of the transition state increases more rapidly than that of the MARI. This ratio effectively cancels in rate equations before the formation of extended H_2O networks because both MARI and transition states reside on the periphery of $(H_3O^+)(H_2O)_n$ clusters, and only become solvated after these clusters have reached their maximum size, as indicated by AIMD and metadynamics simulations. Inhibition by H_2O in the ideal regime (up to -1 order, <10 kPa H_2O) is

therefore accounted for by solvation of H^+ within clusters of increasing molecularity as H_3O^+, as shown previously in H_2O–organic solvent mixtures;[66,67] however, extended hydrogen-bonded networks that solvate the MARI and transition state clusters after they are formed lead to more severe inhibition than that caused by stabilization of H^+ alone.

The less effective solvation of the transition state that leads to more rapidly increasing values of $\gamma_\ddagger$ relative to γ_{EW_n} is likely a consequence of the inability of the non-polar ethyl groups of ethanol molecules to participate in hydrogen bonding networks. The transition state engages the hydroxyl groups of both C_2H_5OH molecules as nucleophile and leaving groups, and thus both ethyl groups present at the transition state may disrupt hydrogen bonds in surrounding H_2O networks. In contrast, the $(C_2H_5OH)(H_3O^+)(H_2O)_{4-5}$ MARI contains only one non-polar ethyl group, which disrupts surrounding H_2O networks to a lesser extent than the two ethyl groups of the transition state. This analysis is conceptually similar to that of the activation volume[114–117] in liquid-phase reactions or the activation area on two-dimensional surfaces,[118] where increasing pressures and concomitant increasing densification of the solvent phase destabilizes transition states with positive activation volume, according to the empirical equation:[115]

$$\left(\frac{\partial \ln(k)}{\partial P}\right)_T = \frac{-\Delta v^\ddagger}{RT} \tag{15}$$

where $\Delta v^\ddagger$ is the (molar) activation volume of the transition state relative to its precursor(s). Here, the apparent activation volume is positive because transition states include two adsorbed C_2H_5OH molecules while the MARI species only includes one. The disruption of extended hydrogen-bonded networks by transition states has also been implicated in aqueous-phase glucose-fructose isomerization[34] and 1-octene epoxidation catalysis[28] in Ti-Beta zeolites, where zeolites of different hydrophobicity enabled including or excluding H_2O networks or clusters, but not systematic variation of the intrapore structure of these networks between these two limiting conditions.

Here, we have demonstrated that gas-phase kinetic measurements and spectroscopic characterizations with co-fed solvent molecules under conditions that lead to intrapore condensation of extended liquid-like networks enable quantifying the thermodynamic nonidealities introduced by the solvation of kinetically relevant intermediates and transition states within confining environments, which are inaccessible to measurements performed in the liquid phase. These thermodynamic activity coefficients contain molecular information about the disruption and reorganization of hydrogen-bonded water networks by transition states that are larger and less polar than their relevant precursors. This approach can be used to investigate the effects of the shape and size of confining pore environments on stabilizing water structures, which in turn influence the solvation of reactive intermediates and transition states, independent of other phenomena that also change concomitantly with pore architecture, such as reactant coverage regimes or co-solvent interactions that often complicate precise mechanistic interpretation of measured rate data.

2.6. Influence of pore topology on solvation effects

The generality of non-ideal solvation effects in confined liquid-like H_2O networks, and the effect of the topology of the pores that confine them, was explored at 373 K in different zeolite frameworks (CHA, AEI, FAU, TON, MFI) and in a less-confined solid acid ($H_3PW_{12}O_{40}$/Si-MCM-41), whose pore topologies and acid site densities are described in Table 2. The values of k_{first} were quantified at H_2O pressures between 0.1–75 kPa and reported in Fig. 7a. Regardless of confining environment, bimolecular ethanol dehydration turnover rates (373 K, per H^+) on Brønsted acids were inhibited by H_2O, and this inhibition could be described by eqn (6) only at lower H_2O pressures, which enabled quantifying $k_3K_2K_4^{-1}$ values in regimes where k_{first} values were -1 order in H_2O. These lumped rate and equilibrium constants reflect the free energy of the confined bimolecular dehydration transition state ($[C_2H_5O(H)\cdots(C_2H_5)^+\cdots OH_2(H_2O)_n]^\ddagger$) and gas-phase water with respect to the confined $(C_2H_5OH)(H_3O^+)(H_2O)_n$ MARI and gas-phase ethanol (Scheme 1). Gaseous species are insensitive to confinement within zeolite pores and their stabilities are unaffected by changes in topology, while the MARI and transition state are expected to be stabilized to different extents by van der Waals contacts within confining micropores of different dimensions.[120] The microporous voids where the MARI and transition state reside can be

Table 2 Elemental compositions, micropore volumes, H^+ densities, and topological descriptors of Brønsted acidic solids

Sample	Si/Al[a]	V_{micro}[b]/cm^3 g^{-1}	H^+/Al (NH_4^+)[c]	H^+/Al (DTBP)[d]	d_{PL}[e]/nm	d_{LC}[f]/nm	Undulation parameter[g]
H-Al-CHA	15	0.21[h]	0.98	—	0.372	0.737	0.505
H-Al-AEI	9.5	0.20[h]	0.85	—	0.384	0.733	0.524
H-Al-FAU	56	0.30	0.35	0.88	0.735	1.124	0.654
H-Al-MFI	43	0.13	0.85	—	0.470	0.636	0.739
H-Al-TON	43	0.05	0.77	—	0.511	0.571	0.895
H-Al-Beta-F(2.0)	23	0.22	0.75	0.54	0.595	0.668	0.891
HPW/Si-MCM-41	11[i]	—	—	1.6[j]	3.8[k]	3.8[k]	1.0

[a] Determined by AAS. [b] Determined by N_2 adsorption minimum in $\partial V_{ads}/\partial \log(P/P_0)$. [c] Determined by TPD of NH_3 after aqueous-phase ion exchange with 1 M NH_4NO_3, 24 h, 353 K. [d] Determined by in situ 2,6-di-tert-butylpyridine titration during ethanol dehydration catalysis (378 K, 5 kPa C_2H_5OH, 1 kPa H_2O). [e] Pore-limiting diameter.[119] [f] Diameter of largest included sphere.[119] [g] Undulation parameter = d_{PL}/d_{LC}. [h] Determined by Ar adsorption minimum in $\partial V_{ads}/\partial \log(P/P_0)$. [i] W/P ratio quantified by ICP. [j] H^+/POM. [k] Average of pore-size distribution determined by N_2 adsorption isotherm and NLDFT (Fig. S30, ESI).
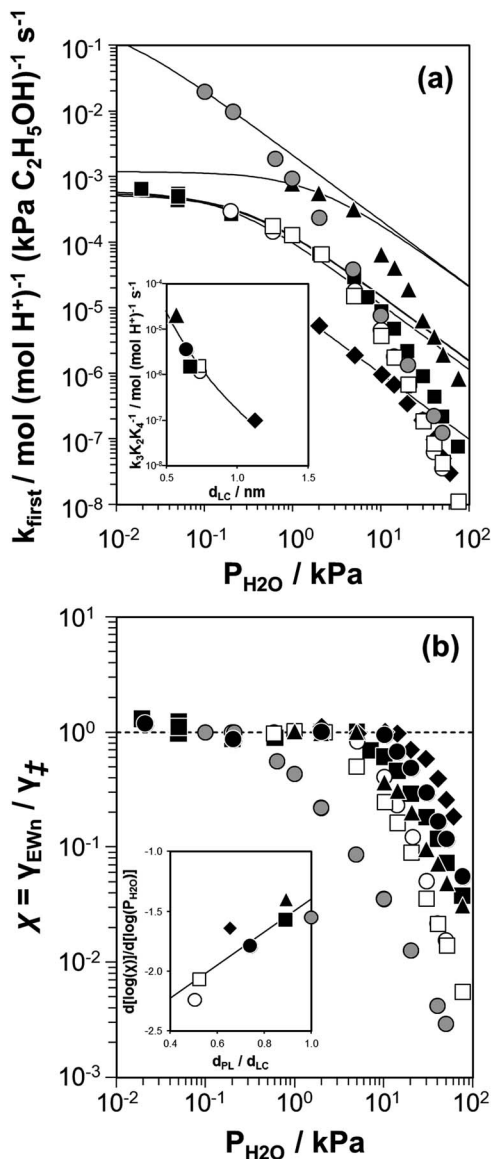
Fig. 7 (a) Apparent first-order bimolecular ethanol dehydration rate constant (per H^+, 373 K) and (b) activity coefficient ratio ($\chi = \gamma_{EW_n}/\gamma_{\ddagger}$) from eqn (7), as a function of H_2O pressure on H-Al-Beta-F(2.0) (■), H-Al-TON (▲), H-Al-FAU (◆), H-Al-MFI (●), H-Al-AEI (□), H-Al-CHA (○), and HPW/Si-MCM-41 (◕). Solid lines in (a) reflect regression of measured rate constants to eqn (7). Inset (a): dependence of $k_3 K_2 K_4^{-1}$ values on the largest included sphere diameter of zeolite pores (d_{LC}). Inset (b): slopes of the data sets in (b) in the high water pressure limit, as a function of the channel undulation parameter (d_{PL}/d_{LC}). Solid lines in both insets are to guide the eye.

reasonably approximated by the diameter of the largest contained sphere within the zeolite, d_{LC}.[119]

Values of $k_3 K_2 K_4^{-1}$ systematically decrease with increasing d_{LC} (Fig. 7a inset), consistent with the expectation that bimolecular dehydration transition states are preferentially stabilized within confining pore environments relative to $(C_2H_5OH)(H_3O^+)(H_2O)_n$ MARI, which are smaller in size and therefore benefit less than transition states do from van der Waals contacts (Scheme 1). The HPW/Si-MCM-41 sample is not

included in this correlation because POMs are stronger acids than zeolites (deprotonation energy (DPE) = 1087 kJ mol^{-1} for HPW[121] < 1201 ± 11 kJ mol^{-1} for H-Al-zeolites[122]), whose acid strength is independent of topology.[122] Notably, values of $k_3 K_2 K_4^{-1}$ are similar in CHA, AEI, and Beta, suggesting that reacting species are confined within the larger cages of CHA and AEI (d_{LC} = 0.73–0.74 nm) that are similar in size to the channels of Beta (d_{LC} = 0.67 nm), rather than their constrained 8-MR windows (pore-limiting diameter, d_{PL} = 0.37–0.38 nm, Table 2). While the kinetic behavior of zeolites in regimes where $\chi = 1$ is consistent with well-known principles of stabilization by attractive dispersion forces in confining environments, it is unclear whether the condensation of liquid-like water within micropores may attenuate or enhance the effects of confinement.

Measured χ values are shown as a function of H_2O pressure (373 K) in Fig. 7b. Brønsted acid zeolites begin to deviate from χ values of unity in the range ∼5–20 kPa H_2O, while HPW/Si-MCM-41 shows deviations in χ starting at ∼1 kPa of H_2O. The earlier onset pressure of deviations observed on HPW/Si-MCM-41 may be related to its higher acid strength, which we surmise would stabilize H_3O^+ liberated from the conjugate anion at lower gas-phase H_2O chemical potentials; a systematic study using POMs of different acid strength would provide clarification, but is beyond the scope of this investigation. The earlier onset of deviations in HPW/Si-MCM-41 has striking consequences for measured k_{first} values, which are more than one order of magnitude higher than on H-Al-Beta zeolites in the $\chi = 1$ regime, but decrease to similar values between 10–75 kPa H_2O (Fig. 7a), indicating that solvation by extended hydrogen-bonded water networks attenuates any benefits of acid strength conferred by forming a more stable solid conjugate anion.[85] The presence of these extended hydrogen-bonded water networks was observed as increasing $\nu(OH)$ IR peak areas below 3200 cm^{-1} on H-Al-zeolites and HPW/Si-MCM-41 at 373 K between 10–75 kPa H_2O (Fig. S57–S63, ESI†), as observed on H-Al-Beta-F (Fig. 4). Similar liquid-phase reactivity of solid acids of different strength was previously observed for dehydration of xylose to furfural (418 K, 0.15 M in H_2O or γ-valerolactone solvent) with H-Al-Beta zeolites and $H_4SiW_{12}O_{40}$ clusters in solution.[66]

In addition to the onset pressure of deviations in χ, its dependence on H_2O pressure was compared among samples and quantified as the slope of the data in Fig. 7b in the high pressure limit, $d[\log(\chi)]/d[\log(P_{H_2O})]$. The value of $d[\log(\chi)]/d[\log(P_{H_2O})]$ is numerically equivalent to the reaction order of k_{first} in H_2O plus one, because χ reflects the deviation from an apparent −1 kinetic order in water. The value of $d[\log(\chi)]/d[\log(P_{H_2O})]$ was ca. −1.5 for Beta, TON, and FAU zeolites, and HPW/MCM-41, while it was −1.8 for MFI zeolites, and less than −2 for CHA and AEI zeolites (Fig. 7b inset). The values of $d[\log(\chi)]/d[\log(P_{H_2O})]$ do not correlate with confinement (d_{LC}, Fig. S28, ESI†) and are similar regardless of acid strength (cf. HPW/MCM-41, Beta, TON, FAU). In contrast, both CHA and AEI zeolites show χ values that decrease more sharply with H_2O pressure, and possess small-pore window-cage motifs different from the other structures characterized by channels (Beta, TON,

MCM-41) or large-pore supercages (FAU). The MFI topology lies between these two cases because it possesses channels (d_{PL} = 0.470 nm) that meet at less-confined intersections (d_{LC} = 0.636 nm). These topological differences have been described previously as the undulation parameter,[123,124] expressed as d_{PL}/d_{LC} (Table 2), which correlates with the values of d[log(χ)]/d [log(P_{H_2O})] (Fig. 7b inset). The undulation parameter has been invoked to account for the preferential retention of certain reaction products that can undergo additional reactions before egress from the crystallite because of the difficulty of egress through more confining windows.[123,124] We hypothesize that χ values deviate more severely from unity within small-pore cage-window topologies (CHA, AEI) than in channel-based topologies (Beta, TON, MCM-41) because extended H_2O networks encounter additional barriers to reorganization when their structures are constrained into adjacent cages through confining windows. The different dependence of water inhibition on zeolite framework topology in regimes that approach liquid-phase catalysis (373 K, 10–75 kPa) and the deviation of k_{first} values from those expected based on measurements in low water-coverage regimes indicate that the structures of adsorbed solvents within micropores of different size and shape play a significant role in determining their reactivity.

3. Conclusions

Ethanol dehydration turnover rates to form diethyl ether (373 K, per H^+) are quantified on H-Al-Beta-F zeolites with 0.11–2.0 H^+ per unit cell under conditions that lead to acid sites with MARI consisting of one C_2H_5OH molecule and increasing amounts of H_2O (2×10^{-3} to 10 kPa C_2H_5OH, 0–75 kPa H_2O), reflected in turnover rates that are first-order in C_2H_5OH and systematically decrease with H_2O pressure. First-order rate constants (373 K, per H^+) show −1 order dependences on H_2O pressure at less than 10 kPa H_2O because one water in water–ethanol–hydronium clusters must be displaced by ethanol to form the S_N2 transition state that eliminates diethyl ether, but they are inhibited more severely at higher H_2O pressures (10–75 kPa).

Under conditions of severe H_2O inhibition (373 K, 10–75 kPa H_2O, 0.05–4.6 kPa C_2H_5OH), in situ IR spectra and AIMD simulations reveal stabilization of $(C_2H_5OH)(H_3O^+)(H_2O)_{4–5}$ clusters and, at even higher water pressures, hydrogen-bonded H_2O networks that solvate such clusters. AIMD demonstrates that H^+ are solvated as H_3O^+ within the MARI, and that C_2H_5OH adsorption becomes less favorable at higher water pressures as it disrupts more extensive hydrogen bonds within clusters of higher molecularity. Metadynamics simulations indicate that the corresponding transition states reside on the periphery of H_2O clusters and thus are formed without desorbing H_2O from clusters beyond the one H_2O required to be displaced by C_2H_5OH at the transition state. Non-ideal thermodynamic formalisms describe the different solvation of MARI and transition states by extended H_2O networks, which are disrupted to a greater extent by the transition state because it contains one additional non-polar ethyl moiety that is less effective at H-bonding, leading to severe inhibition of turnover rates; such

effects are reminiscent of liquid-phase reactions with positive activation volume.

The different solvation of MARI and transition states by water networks prevails among Brønsted acid zeolites of different topology (FAU, TON, MFI, CHA, AEI), whose micropore shapes influence the severity of H_2O inhibition by influencing the ease of solvent reorganization within channel or window-cage motifs. Similar extended H-bonded H_2O structures have also been identified within the pores of hydrophilic metal–organic frameworks[125,126] whose diverse topologies may stabilize an even broader range of solvent structures. The theoretical techniques developed here enable more direct comparison with experimental kinetics using solvent models based on locally stable phases at catalyst active sites. Greater insights into the structure of solvents confined within porous voids are provided by kinetics, spectroscopy, and theoretical calculations of solvated reaction coordinates under conditions that approach intrapore condensation, because this approach allows systematic variation of confined solvent structures. This study highlights the kinetic relevance of water- and water-reactant clusters at H^+ active sites in aqueous-phase Brønsted acid catalysis, and the extended H-bonded networks that surround them, which are disrupted to different extents by reacting moieties of different size and chemical functionality, and which reorganize differently within pores of varied geometry.

4. Methods and materials

4.1. Zeolite synthesis and post-synthetic treatments

H-Al-Beta-F zeolites were hydrothermally synthesized in fluoride medium with a wide range of Al contents by adapting a procedure reported by Camblor et al.[77] An Al-Beta-OH zeolite sample was hydrothermally synthesized in hydroxide medium as reported by Chang et al.[127] These samples are denoted H-Al-Beta-X(Y), where X is the mineralizing agent in the gel (F, OH), and Y is the number of H^+ per unit cell quantified by temperature-programmed desorption of NH_3 (Section S.1.5, ESI†). H-Al-Beta-F zeolites were dealuminated in concentrated nitric acid, denoted deAl-Beta-F. The other H-zeolite samples were sourced commercially (TON, MFI, FAU), or reported in prior publications (CHA,[128] AEI[129]). Phosphotungstic acid polyoxometalate clusters were supported on Si-MCM-41 using incipient wetness impregnation. Full synthetic details are provided in Section S.1.1 of the ESI.†

4.2. Characterization of zeolites

Routine characterizations, including powder X-ray diffraction, N_2 and H_2O adsorption, atomic absorption spectroscopy, inductively coupled plasma optical emission spectrometry (ICP-OES), and temperature-programmed desorption of NH_3, are described in Section S.1.2–S.1.5 of the ESI.†

Infrared spectra of H_2O adsorbed within zeolites were collected as a function of relative pressure (P/P_0 = 0.1–0.75) using procedures described previously.[34,75] Spectra were collected at 293 K using a quartz cell and heated block assembly[130] described in our prior work,[34,75] and spectra were

collected in separate experiments at 373 K using a low-dead-volume cell developed by Ribeiro and coworkers.[131] Additional details are provided in Section S.1.6 of the ESI.†

4.3. Ethanol dehydration kinetics

The kinetics of bimolecular ethanol dehydration to diethyl ether were measured in a differential packed-bed reactor system described previously.[60,132] The pressures of C_2H_5OH (2×10^{-3} to 10 kPa) and H_2O (0–75 kPa) were varied non-systematically over the course of the experiment. No deactivation was detected over the course of kinetic measurements (~7–21 days), verified by periodically returning to a reference condition (5 kPa C_2H_5OH, 50 kPa H_2O). At the end of kinetic measurements on H-Al-Beta, H-Al-FAU, and HPW/Si-MCM-41 catalysts, H^+ were titrated *in situ* with 2,6-di-*tert*-butylpyridine (DTBP) at 378 K. After suppression of measured rates, the irreversibility of titration was confirmed by observing no recovery of measured rates or desorption of DTBP after returning the DTBP-free stream to the reactor. Additional details are provided in Section S.1.7 of the ESI.†

4.4. Gas-phase DFT

Static DFT calculations were performed using VASP[133–135] and are similar to those we have reported previously.[59] The BEEF-vdW functional was used along with a 520 eV cutoff energy, and a force convergence criteria of 0.02 eV Å^{-1} where lattice atoms were all unconstrained. The projector augmented wave (PAW) pseudopotentials were included. Transition states were obtained using the climbing-image nudged elastic band (CI-NEB) method developed by Henkelman.[136–138] As a result of the large diffusion contribution in gas-phase adsorbates, the entropies of reactive intermediates were calculated using the Campbell–Sellers equation,[139,140] where adsorbates were treated as a 2-D gas. The reported energies of each intermediate and transition state reflect the lowest-energy configuration among multiple considered configurations. Additional details are provided in Section S.1.8 of the ESI.†

4.5. *Ab initio* molecular dynamics

AIMD simulations were performed with VASP, with an NVT Nosé–Hoover thermostat.[141,142] Water structures were heated, and then equilibrated at 373 K for at least 10 ps at a timestep of 1 ps. Production runs were performed for 20 ps. All framework atoms were unconstrained. It was assumed that the proton entropy is constant, and so at each timestep the acidic proton was removed in post-production. The root-mean-squared (RMS) diffusion of each water molecule was calculated according to the technique of Alexopoulos *et al.*[108] to yield the 3-D translational entropy of water. The same technique was used to calculate the translational entropy of ethanol molecules introduced into the system. See Section S.2.8 of the ESI† for additional discussion of the entropy calculations and contributions from rotational and vibrational degrees of freedom, which were not included. Additional methodological details are provided in Section S.1.9 of the ESI.†

4.6. Metadynamics

Metadynamics simulations were performed in VASP using the same pseudopotentials, energy cutoff, and K-point grid as the AIMD simulations. The thermostat and masses were the same as the AIMD calculations. The positions and trajectories from the AIMD thermodynamic calculations were used to ensure a well-equilibrated simulation. The collective variables (CVs) were defined to be a carbon–oxygen bond distance of a carbon belonging to one ethanol and a carbon–oxygen bond distance of the same carbon and the oxygen atom of the second ethanol. Gaussian hills were added every 70 fs with a height of 50 meV and width of 75 meV for the first 140 ps. For the last 35 ps the hill height was increased to 100 meV with a width of 150 meV. Hills were added with the same frequency. The total metadynamics simulation was 175 ps with 2500 Gaussian hills inserted in the free energy surface. From the transition state configurations obtained from metadynamics, a constrained molecular dynamics simulation was performed with the C–O bond distances constrained to the saddle point. The duration of this simulation was 18 ps. Additional details are provided in Section S.1.10 of the ESI.†

Conflicts of interest

There are no conflicts to declare.

Acknowledgements

References

1 G. Li, B. Wang and D. E. Resasco, *ACS Catal.*, 2020, **10**, 1294–1309.

2 J. Resasco, L. D. Chen, E. Clark, C. Tsai, C. Hahn, T. F. Jaramillo, K. Chan and A. T. Bell, *J. Am. Chem. Soc.*, 2017, **139**, 11277–11287.

3 Z. K. Goldsmith, Y. C. Lam, A. V. Soudackov and S. Hammes-Schiffer, *J. Am. Chem. Soc.*, 2019, **141**, 1084–1090.

4 M. N. Jackson, O. Jung, H. C. Lamotte and Y. Surendranath, *ACS Catal.*, 2019, **9**, 3737–3743.

5 X. Yang, J. Nash, N. Oliveira, Y. Yan and B. Xu, *Angew. Chem., Int. Ed.*, 2019, **58**, 17718–17723.

6 X. Zhao and Y. Liu, *J. Am. Chem. Soc.*, 2020, **142**, 5773–5777.

7 B. N. Zope, D. D. Hibbitts, M. Neurock and R. J. Davis, *Science*, 2010, **330**, 74–78.

8 N. M. Wilson and D. W. Flaherty, *J. Am. Chem. Soc.*, 2016, **138**, 574–586.

9 J. Saavedra, C. J. Pursell and B. D. Chandler, *J. Am. Chem. Soc.*, 2018, **140**, 3712–3723.

10 D. Muñoz-Santiburcio, M. F. Camellone and D. Marx, *Angew. Chem., Int. Ed.*, 2018, **57**, 3327–3331.

11 G. Yang, S. A. Akhade, X. Chen, Y. Liu, M.-S. Lee, V.-A. Glezakou, R. Rousseau and J. A. Lercher, *Angew. Chem., Int. Ed.*, 2019, **58**, 3527–3532.

12 K. B. Sravan Kumar, T. N. Whittaker, C. Peterson, L. C. Grabow and B. D. Chandler, *J. Am. Chem. Soc.*, 2020, **142**, 5760–5772.

13 E. Iglesia, *Appl. Catal., A*, 1997, **161**, 59–78.

14 A. K. Dalai, T. K. Das, K. V. Chaudhari, G. Jacobs and B. H. Davis, *Appl. Catal., A*, 2005, **289**, 135–142.

15 D. D. Hibbitts, B. T. Loveless, M. Neurock and E. Iglesia, *Angew. Chem., Int. Ed.*, 2013, **52**, 12273–12278.

16 F. Anaya and D. E. Resasco, *ACS Catal.*, 2020, **10**, 4433–4443.

17 Y. T. Kim, J. P. Chada, Z. Xu, Y. J. Pagan-Torres, D. C. Rosenfeld, W. L. Winniford, E. Schmidt and G. W. Huber, *J. Catal.*, 2015, **323**, 33–44.

18 I. Agirrezabal-Telleria and E. Iglesia, *J. Catal.*, 2017, **352**, 505–514.

19 I. Agirrezabal-Telleria, I. Luz, M. A. Ortuño, M. Oregui-Bengoechea, I. Gandarias, N. López, M. A. Lail and M. Soukri, *Nat. Commun.*, 2019, **10**, 2076.

20 S. Ghosh, K. V. Ramanathan and A. K. Sood, *Europhys. Lett.*, 2004, **65**, 678.

21 Q. Chen, J. L. Herberg, G. Mogilevsky, H.-J. Wang, M. Stadermann, J. K. Holt and Y. Wu, *Nano Lett.*, 2008, **8**, 1902–1905.

22 T. Ohba, *Angew. Chem., Int. Ed.*, 2014, **53**, 8032–8036.

23 S. Dalla Bernardina, E. Paineau, J.-B. Brubach, P. Judeinstein, S. Rouzière, P. Launois and P. Roy, *J. Am. Chem. Soc.*, 2016, **138**, 10437–10443.

24 P. W. Snyder, M. R. Lockett, D. T. Moustakas and G. M. Whitesides, *Eur. Phys. J.: Spec. Top.*, 2014, **223**, 853–891.

25 G. Langhendries, D. E. De Vos, G. V. Baron and P. A. Jacobs, *J. Catal.*, 1999, **187**, 453–463.

26 M. G. Clerici, *Top. Catal.*, 2001, **15**, 257–263.

27 N. A. Grosso-Giordano, C. Schroeder, A. Okrut, A. Solovyov, C. Schöttle, W. Chassé, N. Marinković, H. Koller, S. I. Zones and A. Katz, *J. Am. Chem. Soc.*, 2018, **140**, 4956–4960.

28 D. T. Bregante, A. M. Johnson, A. Y. Patel, E. Z. Ayla, M. J. Cordon, B. C. Bukowski, J. Greeley, R. Gounder and D. W. Flaherty, *J. Am. Chem. Soc.*, 2019, **141**, 7302–7319.

29 N. A. Grosso-Giordano, A. S. Hoffman, A. Boubnov, D. W. Small, S. R. Bare, S. I. Zones and A. Katz, *J. Am. Chem. Soc.*, 2019, **141**, 7090–7106.

30 R. Gounder and M. E. Davis, *J. Catal.*, 2013, **308**, 176–188.

31 R. Gounder and M. E. Davis, *ACS Catal.*, 2013, **3**, 1469–1476.

32 J. W. Harris, M. J. Cordon, J. R. Di Iorio, J. C. Vega-Vila, F. H. Ribeiro and R. Gounder, *J. Catal.*, 2016, **335**, 141–154.

33 J. C. Vega-Vila, J. W. Harris and R. Gounder, *J. Catal.*, 2016, **344**, 108–120.

34 M. J. Cordon, J. W. Harris, J. C. Vega-Vila, J. S. Bates, S. Kaur, M. Gupta, M. E. Witzke, E. C. Wegener, J. T. Miller, D. W. Flaherty, D. D. Hibbitts and R. Gounder, *J. Am. Chem. Soc.*, 2018, **140**, 14244–14266.

35 N. Y. Chen, *J. Phys. Chem.*, 1976, **80**, 60–64.

36 M. Hunger, J. Kärger, H. Pfeifer, J. Caro, B. Zibrowius, M. Bülow and R. Mostowicz, *J. Chem. Soc., Faraday Trans. 1*, 1987, **83**, 3459–3468.

37 J. Stelzer, M. Paulus, M. Hunger and J. Weitkamp, *Microporous Mesoporous Mater.*, 1998, **22**, 1–8.

38 D. H. Olson, W. O. Haag and W. S. Borghard, *Microporous Mesoporous Mater.*, 2000, **35–36**, 435–446.

39 A. Zecchina, F. Geobaldo, G. Spoto, S. Bordiga, G. Ricchiardi, R. Buzzoni and G. Petrini, *J. Phys. Chem.*, 1996, **100**, 16584–16599.

40 M. Krossner and J. Sauer, *J. Phys. Chem.*, 1996, **100**, 6199–6211.

41 L. Smith, A. K. Cheetham, R. E. Morris, L. Marchese, J. M. Thomas, P. A. Wright and J. Chen, *Science*, 1996, **271**, 799–802.

42 M. Jiménez-Ruiz, D. S. Gahle, T. Lemishko, S. Valencia, G. Sastre and F. Rey, *J. Phys. Chem. C*, 2020, **124**, 5436–5443.

43 A. Vjunov, M. Wang, N. Govind, T. Huthwelker, H. Shi, D. Mei, J. L. Fulton and J. A. Lercher, *Chem. Mater.*, 2017, **29**, 9030–9042.

44 S. Eckstein, P. H. Hintermeier, R. Zhao, E. Baráth, H. Shi, Y. Liu and J. A. Lercher, *Angew. Chem., Int. Ed.*, 2019, **58**, 3450–3455.

45 M. Wang, N. R. Jaegers, M.-S. Lee, C. Wan, J. Z. Hu, H. Shi, D. Mei, S. D. Burton, D. M. Camaioni, O. Y. Gutiérrez, V.-A. Glezakou, R. Rousseau, Y. Wang and J. A. Lercher, *J. Am. Chem. Soc.*, 2019, **141**, 3444–3455.

46 G. Zundel, *Angew. Chem., Int. Ed. Engl.*, 1969, **8**, 499–509.

47 M. Eigen, *Angew. Chem., Int. Ed. Engl.*, 1964, **3**, 1–19.

48 E. S. Stoyanov, I. V. Stoyanova and C. A. Reed, *J. Am. Chem. Soc.*, 2010, **132**, 1484–1485.

49 J. F. Haw, T. Xu, J. B. Nicholas and P. W. Goguen, *Nature*, 1997, **389**, 832–835.

50 K. Chen, J. Damron, C. Pearson, D. Resasco, L. Zhang and J. L. White, *ACS Catal.*, 2014, **4**, 3039–3044.

51 K. Chen, A. Gumidyala, M. Abdolrhamani, C. Villines, S. Crossley and J. L. White, *J. Catal.*, 2017, **351**, 130–135.

52 M. Nielsen, A. Hafreager, R. Y. Brogaard, K. D. Wispelaere, H. Falsig, P. Beato, V. V. Speybroeck and S. Svelle, *Catal. Sci. Technol.*, 2019, **9**, 3721–3725.

53 Z. Zhao, R. Bababrik, W. Xue, Y. Li, N. M. Briggs, D.-T. Nguyen, U. Nguyen, S. P. Crossley, S. Wang, B. Wang and D. E. Resasco, *Nat. Catal.*, 2019, **2**, 431–436.

54 G. Li, B. Wang, B. Chen and D. E. Resasco, *J. Catal.*, 2019, **377**, 245–254.

55 H. Knözinger, *Angew. Chem., Int. Ed. Engl.*, 1968, **7**, 791–805.

56 J. Macht, M. J. Janik, M. Neurock and E. Iglesia, *J. Am. Chem. Soc.*, 2008, **130**, 10369–10379.

57 J. F. DeWilde, H. Chiang, D. A. Hickman, C. R. Ho and A. Bhan, *ACS Catal.*, 2013, **3**, 798–807.

58 M. Kang and A. Bhan, *Catal. Sci. Technol.*, 2016, **6**, 6667–6678.

59 B. C. Bukowski, J. S. Bates, R. Gounder and J. Greeley, *J. Catal.*, 2018, **365**, 261–276.

60 J. S. Bates and R. Gounder, *J. Catal.*, 2018, **365**, 213–226.

61 Y. Zhi, H. Shi, L. Mu, Y. Liu, D. Mei, D. M. Camaioni and J. A. Lercher, *J. Am. Chem. Soc.*, 2015, **137**, 15781–15794.

62 Y. Liu, A. Vjunov, H. Shi, S. Eckstein, D. M. Camaioni, D. Mei, E. Baráth and J. A. Lercher, *Nat. Commun.*, 2017, **8**, 14113.

63 Y. Liu, E. Baráth, H. Shi, J. Hu, D. M. Camaioni and J. A. Lercher, *Nat. Catal.*, 2018, **1**, 141–147.

64 S. Eckstein, P. H. Hintermeier, M. V. Olarte, Y. Liu, E. Baráth and J. A. Lercher, *J. Catal.*, 2017, **352**, 329–336.

65 L. Qi, R. Alamillo, W. A. Elliott, A. Andersen, D. W. Hoyt, E. D. Walter, K. S. Han, N. M. Washton, R. M. Rioux, J. A. Dumesic and S. L. Scott, *ACS Catal.*, 2017, **7**, 3489–3500.

66 M. A. Mellmer, C. Sener, J. M. R. Gallo, J. S. Luterbacher, D. M. Alonso and J. A. Dumesic, *Angew. Chem., Int. Ed.*, 2014, **53**, 11872–11875.

67 M. A. Mellmer, C. Sanpitakseree, B. Demir, P. Bai, K. Ma, M. Neurock and J. A. Dumesic, *Nat. Catal.*, 2018, **1**, 199–207.

68 A. K. Chew, T. W. Walker, Z. Shen, B. Demir, L. Witteman, J. Euclide, G. W. Huber, J. A. Dumesic and R. C. Van Lehn, *ACS Catal.*, 2020, **10**, 1679–1691.

69 N. S. Gould, S. Li, H. J. Cho, H. Landfield, S. Caratzoulas, D. Vlachos, P. Bai and B. Xu, *Nat. Commun.*, 2020, **11**, 1–13.

70 N. S. Gould and B. Xu, *J. Catal.*, 2016, **342**, 193–202.

71 N. S. Gould and B. Xu, *J. Catal.*, 2018, **358**, 80–88.

72 B. M. Murphy, J. Wu, H. J. Cho, J. Soreo, C. Wang, L. Ma and B. Xu, *ACS Catal.*, 2019, **9**, 1931–1942.

73 D. Mei and J. A. Lercher, *AIChE J.*, 2017, **63**, 172–184.

74 D. Mei and J. A. Lercher, *J. Phys. Chem. C*, 2019, **123**, 25255–25266.

75 B. C. Bukowski, J. S. Bates, R. Gounder and J. Greeley, *Angew. Chem., Int. Ed.*, 2019, **58**, 16422–16426.

76 D. T. Bregante and D. W. Flaherty, *ACS Catal.*, 2019, **9**, 10951–10962.

77 M. A. Camblor, A. Corma and S. Valencia, *J. Mater. Chem.*, 1998, **8**, 2137–2145.

78 H. Koller, R. F. Lobo, S. L. Burkett and M. E. Davis, *J. Phys. Chem.*, 1995, **99**, 12588–12596.

79 C. D. Baertsch, K. T. Komala, Y.-H. Chua and E. Iglesia, *J. Catal.*, 2002, **205**, 44–57.

80 R. T. Carr, M. Neurock and E. Iglesia, *J. Catal.*, 2011, **278**, 78–93.

81 T. Bligaard, R. M. Bullock, C. T. Campbell, J. G. Chen, B. C. Gates, R. J. Gorte, C. W. Jones, W. D. Jones, J. R. Kitchin and S. L. Scott, *ACS Catal.*, 2016, **6**, 2590–2602.

82 S. R. Blaszkowski and R. A. van Santen, *J. Am. Chem. Soc.*, 1996, **118**, 5152–5153.

83 C. B. Phillips and R. Datta, *Ind. Eng. Chem. Res.*, 1997, **36**, 4466–4475.

84 H. Chiang and A. Bhan, *J. Catal.*, 2010, **271**, 251–261.

85 W. Knaeble and E. Iglesia, *J. Phys. Chem. C*, 2016, **120**, 3371–3389.

86 R. J. Madon and M. Boudart, *Ind. Eng. Chem. Fundam.*, 1982, **21**, 438–447.

87 D. Mears, *Ind. Eng. Chem. Process Des. Dev.*, 1971, **10**, 541–547.

88 R. Gounder and M. E. Davis, *AIChE J.*, 2013, **59**, 3349–3358.

89 P. A. Thiel and T. E. Madey, *Surf. Sci. Rep.*, 1987, **7**, 211–385.

90 I. Kiricsi, C. Flego, G. Pazzuconi, W. O. Parker Jr, R. Millini, C. Perego and G. Bellussi, *J. Phys. Chem.*, 1994, **98**, 4627–4634.

91 J. A. Lercher and A. Jentys, in *Studies in Surface Science and Catalysis*, ed. H. van B. Jiří Čejka Avelino Corma and F. Schüth, Elsevier, 2007, vol. 168, pp. 435–476.

92 A. Corma, V. Fornés, F. Melo and J. Pérez-Pariente, in *Fluid Catalytic Cracking*, American Chemical Society, 1988, vol. 375, pp. 49–63.

93 A. Zecchina, S. Bordiga, G. Spoto, D. Scarano, G. Spanò and F. Geobaldo, *J. Chem. Soc., Faraday Trans.*, 1996, **92**, 4863–4875.

94 M. F. Claydon and N. Sheppard, *J. Chem. Soc. D*, 1969, 1431–1433.

95 A. G. Pelmenschikov, R. A. van Santen, J. H. M. C. van Wolput and J. Jänchen, in *Studies in Surface Science and Catalysis*, ed. J. Weitkamp, H. G. Karge, H. Pfeifer and W. Hölderich, Elsevier, 1994, vol. 84, pp. 2179–2186.

96 A. G. Pelmenschikov, J. H. M. C. van Wolput, J. Jaenchen and R. A. van Santen, *J. Phys. Chem.*, 1995, **99**, 3612–3617.

97 C. P. Lawrence and J. L. Skinner, *J. Chem. Phys.*, 2002, **118**, 264–272.

98 J. D. Cyran, M. A. Donovan, D. Vollmer, F. S. Brigiano, S. Pezzotti, D. R. Galimberti, M.-P. Gaigeot, M. Bonn and E. H. G. Backus, *Proc. Natl. Acad. Sci. U. S. A.*, 2019, **116**, 1520–1525.

99 J. Schaefer, E. H. G. Backus, Y. Nagata and M. Bonn, *J. Phys. Chem. Lett.*, 2016, **7**, 4591–4595.

100 N. Yang, C. H. Duong, P. J. Kelleher, A. B. McCoy and M. A. Johnson, *Science*, 2019, **364**, 275–278.

101 A. G. Pelmenschikov, R. A. van Santen, J. Janchen and E. Meijer, *J. Phys. Chem.*, 1993, **97**, 11071–11074.

102 M. Sovago, R. K. Campen, G. W. H. Wurpel, M. Müller, H. J. Bakker and M. Bonn, *Phys. Rev. Lett.*, 2008, **100**, 173901.

103 E. A. Raymond, T. L. Tarbuck and G. L. Richmond, *J. Phys. Chem. B*, 2002, **106**, 2817–2820.

104 P. B. Miranda and Y. R. Shen, *J. Phys. Chem. B*, 1999, **103**, 3292–3307.

105 S. Nihonyanagi, S. Yamaguchi and T. Tahara, *J. Am. Chem. Soc.*, 2010, **132**, 6867–6869.

106 A. Myalitsin, S. Urashima, S. Nihonyanagi, S. Yamaguchi and T. Tahara, *J. Phys. Chem. C*, 2016, **120**, 9357–9363.

107 N. Yang, C. H. Duong, P. J. Kelleher and M. A. Johnson, *Nat. Chem.*, 2020, **12**, 159–164.

108 K. Alexopoulos, M.-S. Lee, Y. Liu, Y. Zhi, Y. Liu, M.-F. Reyniers, G. B. Marin, V.-A. Glezakou, R. Rousseau and J. A. Lercher, *J. Phys. Chem. C*, 2016, **120**, 7172–7182.

109 J. Kästner, *Wiley Interdiscip. Rev. Comput. Mol. Sci.*, 2011, **1**, 932–942.

110 B. L. Foley and A. Bhan, *J. Catal.*, 2020, **384**, 231–251.

111 C. Eckert and M. Boudart, *Chem. Eng. Sci.*, 1963, **18**, 144–147.

112 S. I. Sandler, *Chemical, biochemical, and engineering thermodynamics*, John Wiley, Hoboken, N.J, 4th edn, 2006.

113 R. J. Madon and E. Iglesia, *J. Mol. Catal. A: Chem.*, 2000, **163**, 189–204.

114 K. J. Laidler and D. Chen, *Trans. Faraday Soc.*, 1958, **54**, 1026.

115 R. A. Grieger and C. A. Eckert, *Trans. Faraday Soc.*, 1970, **66**, 2579–2584.

116 K. F. Wong and C. A. Eckert, *Trans. Faraday Soc.*, 1970, **66**, 2313–2319.

117 G. A. Lawrance and D. R. Stranks, *Acc. Chem. Res.*, 1979, **12**, 403–409.

118 J. Liu, D. Hibbitts and E. Iglesia, *J. Am. Chem. Soc.*, 2017, **139**, 11789–11802.

119 Ch. Baerlocher and L. B. McCusker, *Database of Zeolite Structures*, http://www.iza-structure.org/databases/, accessed October 14, 2019.

120 R. Gounder and E. Iglesia, *Chem. Commun.*, 2013, **49**, 3491–3509.

121 J. Macht, M. J. Janik, M. Neurock and E. Iglesia, *Angew. Chem., Int. Ed.*, 2007, **46**, 7864–7868.

122 A. J. Jones and E. Iglesia, *ACS Catal.*, 2015, 5, 5741–5755.

123 M. L. Sarazen, E. Doskocil and E. Iglesia, *ACS Catal.*, 2016, 6, 7059–7070.

124 G. Noh, S. I. Zones and E. Iglesia, *J. Catal.*, 2019, **377**, 255–270.

125 A. J. Rieth, A. M. Wright, G. Skorupskii, J. L. Mancuso, C. H. Hendon and M. Dincă, *J. Am. Chem. Soc.*, 2019, **141**, 13858–13866.

126 A. J. Rieth, K. M. Hunter, M. Dincă and F. Paesani, *Nat. Commun.*, 2019, **10**, 4771.

127 C.-C. Chang, Z. Wang, P. Dornath, H. J. Cho and W. Fan, *RSC Adv.*, 2012, **2**, 10475–10477.

128 J. R. Di Iorio and R. Gounder, *Chem. Mater.*, 2016, **28**, 2236–2247.

129 J. D. Albarracin-Caballero, I. Khurana, J. R. D. Iorio, A. J. Shih, J. E. Schmidt, M. Dusselier, M. E. Davis, A. Yezerets, J. T. Miller, F. H. Ribeiro and R. Gounder, *React. Chem. Eng.*, 2017, **2**, 168–179.

130 V. J. Cybulskis, J. W. Harris, Y. Zvinevich, F. H. Ribeiro and R. Gounder, *Rev. Sci. Instrum.*, 2016, **87**, 103101.

131 J. Wang, V. F. Kispersky, W. N. Delgass and F. H. Ribeiro, *J. Catal.*, 2012, **289**, 171–178.

132 J. S. Bates, B. C. Bukowski, J. W. Harris, J. Greeley and R. Gounder, *ACS Catal.*, 2019, **9**, 6146–6168.

133 G. Kresse and D. Joubert, *Phys. Rev. B: Condens. Matter Mater. Phys.*, 1999, **59**, 1758–1775.

134 G. Kresse and J. Hafner, *Phys. Rev. B: Condens. Matter Mater. Phys.*, 1993, **47**, 558–561.

135 G. Kresse and J. Furthmüller, *Phys. Rev. B: Condens. Matter Mater. Phys.*, 1996, **54**, 11169–11186.

136 G. Henkelman, B. P. Uberuaga and H. Jónsson, *J. Chem. Phys.*, 2000, **113**, 9901–9904.

137 G. Henkelman and H. Jónsson, *J. Chem. Phys.*, 2000, **113**, 9978–9985.

138 G. Henkelman and H. Jonsson, *J. Chem. Phys.*, 1999, **111**, 7010–7022.

139 C. T. Campbell and J. R. V. Sellers, *J. Am. Chem. Soc.*, 2012, **134**, 18109–18115.

140 C. T. Campbell and J. R. V. Sellers, *Chem. Rev.*, 2013, **113**, 4106–4135.

141 S. Nosé, *J. Chem. Phys.*, 1984, **81**, 511–519.

142 D. J. Evans and B. L. Holian, *J. Chem. Phys.*, 1985, **83**, 4069–4074.